19

Semiclassical Molecular Dynamics for Spectroscopic Calculations

Riccardo Conte and Michele Ceotto

Dipartimento di Chimica, Università degli Studi di Milano, via Golgi 19, 20133 Milano, Italy

Abstract

We present some historical and recently developed techniques to perform semiclassical spectroscopy calculations with both ground and excited state dynamics. The illustrated topics begin with a derivation of the basic semiclassical van Vleck propagator starting from Feynman's path integral formulation, followed by the description of the initial value representation formalism and a derivation of the Heller–Herman–Kluk–Kay semiclassical propagator. The chapter continues by introducing the time averaging technique and its very recent developments consisting in the multiple coherent, divide-and-conquer, and mixed semiclassical approaches. The main features of each method are described through examples with the intent of helping readers have a gentle learning curve. The chapter ends with a workflow chart, a few representative applications, a summary, and some conclusions.

19.1 Introduction

The primary research goal in the field of spectroscopy is the study of the interaction between light and matter. Depending on the frequency of the radiation, the term spectroscopy is usually specified as ultraviolet (UV), infrared (IR), microwave, and others. The different energy ranges of the radiation actually translate into different targets of investigation. For instance, UV spectroscopy focuses on electronic transitions, IR or Raman spectroscopies on molecular vibrations, and microwave spectroscopy on molecular rotations.

Infrared spectroscopy experiments are important tools for chemical characterization of unknown samples. In fact, peak positions in an IR spectrum are correlated to the molecular structures of the unknown chemical species. Many molecules strongly absorb in the mid-infrared region, defined by frequencies in the range between approximately 400 and 4000 cm^{-1}, with characteristic spectral patterns that can be compared to those of the unknown sample. The spectrum can also be employed in a quantitative way by exploiting peak intensities to estimate the species concentrations once a reference has been set. Furthermore, the width of the peaks can provide useful insights about the environment in which the molecule is embedded including pH conditions and the presence of hydrogen bonding. Finally, the experimental technique is fast and has enough sensitivity to require just a minimum amount of material.

Quantum Chemistry and Dynamics of Excited States: Methods and Applications,
First Edition. Edited by Leticia González and Roland Lindh.

However, the assignment of experimental spectra may become difficult when the complexity or dimensionality of molecular systems increases. Theoretical simulations can provide the necessary support by identifying spectral features with more confidence and relating them to the actual molecular motion. To this end, every theoretical method has to reconcile two different objectives. First, it must describe quantum effects like zero-point energies, overtones, and resonances, which cannot be neglected in spectroscopy. Secondly, it should be sufficiently manageable to be employed also for high dimensional systems.

The starting point of quantum theoretical spectroscopy is the time-independent eigenvalue equation $\hat{H}\Psi(\vec{r},\vec{R}) = E\Psi(\vec{r},\vec{R})$ because, once eigenvalues and eigenvectors of the molecular Hamiltonian are known, frequencies of vibration and absorption spectra can be determined. The general molecular Hamiltonian (neglecting spin-orbit interactions, and indicating electronic coordinates with $\vec{r}$ and nuclear ones with $\vec{R}$) can be written as a sum of five terms

$$\hat{H} = \hat{T}_N(\vec{R}) + \hat{T}_e(\vec{r}) + \hat{V}_{eN}(\vec{r},\vec{R}) + \hat{V}_{NN}(\vec{R}) + \hat{V}_{ee}(\vec{r}) \tag{19.1}$$

corresponding to the kinetic energies of nuclei and electrons and to the electron–nuclei, nuclei–nuclei, and electron–electron interaction potential energies [1]. The Hamiltonian is not separable into a nuclear and an electronic part due to the presence of $\hat{V}_{eN}(\vec{r},\vec{R})$ which makes the original eigenvalue problem difficult to solve. This interaction term is large and cannot be neglected, so in order to separate nuclear and electronic motions an approximation must be invoked. This is known as the Born–Oppenheimer approximation (for details see Chapter 1). Solution of the electronic problem leads to the construction of the potential energy surface for the system. Since the problem is solved at a discrete number of nuclear configurations, an analytical form of the global surface is obtained only upon application of a fitting procedure, which may be quite a difficult task and often constitutes a research topic on its own [2]. Furthermore, for each electronic state a different potential energy surface can be constructed.

The eigenvalues of the vibrational Hamiltonian associated with a specific electronic state are the vibrational energy levels E_k, starting with the zero-point one (E_0), from which it is straightforward to compute the frequencies of all spectral transitions. For instance, the frequency of the transition between the ground state and the generic k state with energy E_k is given by the difference $(E_k - E_0)/\hbar$. As for intensities, if the eigenfunctions are available, then (at least in principle) all dipole matrix elements $\mu_{0k} = \langle\Psi_0|\hat{\mu}|\Psi_k\rangle$ could be calculated and, eventually, the absorption formula

$$I_{abs}(E) \propto E \sum_k \Delta(E - E_k + E_0)\ |\mu_{0k}|^2 \tag{19.2}$$

can be evaluated, where $\Delta(E - E_k + E_0)$ is a bell-shaped function (rigorously a Dirac δ) peaked at $E_k - E_0$. However, the calculation may become prohibitive when the density of vibrational states is very large, which, for high dimensional systems, may happen at low energies.

The goal of this second part of the book is to deal with dynamical approaches. Calculations of vibrational frequencies and absorption spectra can indeed be undertaken by means of a dynamical approach. Specifically, the eigenenergies of the vibrational Hamiltonian can be computed from the Fourier transform of the survival amplitude $\langle\Xi|\Xi(t)\rangle$ of a generic reference state $|\Xi\rangle$. In fact,

$$
\begin{aligned}
I(E) &= \frac{1}{2\pi\hbar}\int_{-\infty}^{+\infty} dt\; e^{\mathrm{i}Et/\hbar}\langle\Xi|\Xi(t)\rangle \\
&= \frac{1}{2\pi\hbar}\int_{-\infty}^{+\infty} dt\; e^{\mathrm{i}Et/\hbar}\langle\Xi|e^{-\mathrm{i}\hat{H}t/\hbar}|\Xi\rangle \\
&= \frac{1}{2\pi\hbar}\int_{-\infty}^{+\infty} dt\; e^{\mathrm{i}Et/\hbar}\sum_k |\langle\Xi|E_k\rangle|^2 e^{-\mathrm{i}E_k t/\hbar} \\
&= \sum_k |\langle\Xi|E_k\rangle|^2\delta(E-E_k).
\end{aligned}
\tag{19.3}
$$

Peaks in the plot of $I(E)$ obtained from numerical implementation of the first relation in Eq. (19.3) are located at the vibrational eigenenergies of the system. Quantum vibrational frequencies are then found easily by scaling the eigenenergies with respect to the ground state energy (i.e., the vibrational zero point energy). A similar expression can be employed for absorption spectra. In fact, in this latter case, the relevant formula is [3]

$$
I_{abs}(E) \propto E\int_{-\infty}^{+\infty} dt\; e^{\mathrm{i}Et/\hbar}\;\langle\hat{\mu}(0)\hat{\mu}(t)\rangle, \tag{19.4}
$$

where the average is over the density matrix of the system.

In the case of a photo-absorption involving two different electronic states (in the low temperature limit) [4]

$$
\langle\hat{\mu}(0)\hat{\mu}(t)\rangle = \langle\Xi_{gs}|\hat{\mu}e^{-i\hat{H}_f t/\hbar}\hat{\mu}e^{i\hat{H}_i t/\hbar}|\Xi_{gs}\rangle, \tag{19.5}
$$

where $|\Xi_{gs}\rangle$ is the ground vibrational state of the lower electronic state, while $\hat{H}_i$ and $\hat{H}_f$ are the nuclear Hamiltonians in the lower and upper electronic surface respectively. This leads to the following working formula

$$
I_{abs}(E) \propto E\int_{-\infty}^{+\infty} dt\; e^{\mathrm{i}(E+E_0)t/\hbar}\;\langle\Theta(0)|\Theta(t)\rangle, \tag{19.6}
$$

where $|\Theta\rangle$ is obtained by applying the electronic transition moment μ to the ground vibrational state $|\Xi_{gs}\rangle$ in the starting electronic state, i.e., $|\Theta\rangle = \hat{\mu}|\Xi_{gs}\rangle$. E_0 in Eq. (19.6) is the energy of $|\Xi_{gs}\rangle$. Within the Condon approximation, the electronic transition moment is taken as a constant. In this way, the initial wave packet for the excited state dynamics ($|\Theta(0)\rangle$) is prepared in a non-stationary state. By evolving it on the excited electronic state, the vibronic absorption spectrum is obtained similarly to power spectra and shows peaks at the energy E of the vibronic transitions. In photoemission calculations formulae are similar. The two surfaces are treated symmetrically, but there is a cubic dependence on the energy in front of the integration [3].

Many different theoretical approaches to spectroscopy have been developed to calculate $I(E)$ and $I_{abs}(E)$. In this chapter we focus on semiclassical (SC) molecular dynamics for spectroscopic calculations [5]. In this context "semiclassical" and "semiclassical dynamics" refer to a set of theories and time-dependent approaches based on an approximate quantum propagator (i.e., the semiclassical propagator) dependent on classical quantities. Therefore, the hallmark of SC dynamics is represented by the possibility to extract quantum features from classical molecular dynamics simulations [6]. This is permitted by the mathematical structure of the semiclassical propagator, which is based on classically evolved trajectories with remarkable ease of computational needs. Due to this property, semiclassical dynamics is a promising tool for high-dimensional applications. Other advantages include the possibility to work in Cartesian coordinates and to use the potential energy

obtained from the electronic problem "as is" and without any further approximation. In particular the potential can be provided in the form of an analytical surface or calculated ab initio on-the-fly for the whole dynamics. Finally, being based on classical dynamics, semiclassical methods may provide a more intuitive picture with respect to quantum approaches.

In this chapter devoted to SC dynamics we illustrate first the derivation of the basic semiclassical propagator as a stationary-phase approximation to Feynman's path integral formulation of quantum mechanics. Then the Heller–Herman–Kluk–Kay propagator is derived. It serves as the starting point for developing the multiple coherent and divide-and-conquer techniques, which are necessary to extend the applicability of semiclassical spectroscopy to high dimensional systems. These techniques are described theoretically and through examples that guide the reader in their application. We introduce also another family of semiclassical propagators known as "thawed Gaussian propagators" and a promising approach to condensed phase spectroscopy, before moving to applications concerning vibrational and vibronic spectroscopy. The methods presented can be applied to studies involving both ground-state and excited-state dynamics. Some general conclusions end the chapter.

19.2 From Feynman's Path Integral to van Vleck's Semiclassical Propagator

Among the many alternative derivations of the semiclassical propagator [7–9], perhaps the most intuitive one originates from Feynman's path integral formulation of the exact quantum propagator [10]. For more information on Feynman's propagator see Chapter 20.

We start from the observation that the differential Schrödinger equation

$$i\hbar\frac{\partial|\Xi\rangle}{\partial t} = \hat{H}|\Xi\rangle \;\rightarrow |\Xi(t)\rangle = e^{-i\hat{H}t/\hbar}|\Xi(0)\rangle \tag{19.7}$$

can be written in the path integral form by projecting the state $|\Xi\rangle$ onto the coordinate $\vec{q}$-space

$$\Xi(\vec{q}'(t)) \equiv \langle\vec{q}'|\Xi(t)\rangle = \langle\vec{q}'|e^{-i\hat{H}t/\hbar}|\Xi(0)\rangle = \int_{-\infty}^{+\infty} d\vec{q}_0\langle\vec{q}'|e^{-i\hat{H}t/\hbar}|\vec{q}_0\rangle\langle\vec{q}_0|\Xi(0)\rangle. \tag{19.8}$$

Insertion of the identity $\int_{-\infty}^{+\infty} d\vec{q}_0|\vec{q}_0\rangle\langle\vec{q}_0|$ into Eq. (19.8) introduces the idea of quantum propagation as the summation over all possible values in $\vec{q}$ – space of the probability amplitude $\langle\vec{q}'|e^{-i\hat{H}t/\hbar}|\vec{q}_0\rangle$ matrix times the state vector $\langle\vec{q}_0|\Xi(0)\rangle$. The focus for solving the quantum propagation is now shifted to a suitable representation of the probability amplitude, instead of the wave function calculation as originally in Eq. (19.7). The first step consists in breaking N times the total time-evolution interval into infinitesimal $\Delta t = t/N$ time slices

$$\langle\vec{q}'|e^{-i\hat{H}t/\hbar}|\vec{q}_0\rangle = \lim_{\Delta t\to 0}\langle\vec{q}'|(e^{-i\hat{H}\Delta t/\hbar})^N|\vec{q}_0\rangle = \lim_{\Delta t\to 0}\langle\vec{q}'|(e^{-i\hat{T}\Delta t/\hbar}e^{-i\hat{V}\Delta t/\hbar})^N|\vec{q}_0\rangle, \tag{19.9}$$

where $\hat{T}$ is the kinetic energy operator, $\hat{V}$ the potential energy one, and the last equality is often referred to as the Suzuki–Trotter decomposition formula. The power of N can be interpreted as a product of N terms, so the next step consists in the insertion of $N-1$ quantum mechanical identities

$$\begin{aligned}\langle\vec{q}'|e^{-i\hat{H}t/\hbar}|\vec{q}_0\rangle = \lim_{\Delta t\to 0}\int_{-\infty}^{+\infty} d\vec{q}_1 \ldots \int_{-\infty}^{+\infty} d\vec{q}_{N-1}\langle\vec{q}'|(e^{-i\hat{T}\Delta t/\hbar}e^{-i\hat{V}\Delta t/\hbar})|\vec{q}_{N-1}\rangle \\ \times\langle\vec{q}_{N-1}|(e^{-i\hat{T}\Delta t/\hbar}e^{-i\hat{V}\Delta t/\hbar})|\vec{q}_{N-2}\rangle\cdots\langle\vec{q}_1|(e^{-i\hat{T}\Delta t/\hbar}e^{-i\hat{V}\Delta t/\hbar})|\vec{q}_0\rangle.\end{aligned} \tag{19.10}$$

In the time limit $\Delta t \to 0$ the potential can be approximated to a constant, the value being that of the potential at the mid-point between the two coordinates of each bracket in Eq. (19.10). The effect is twofold. On the one hand the exponential involving the potential can be evaluated straightforwardly. On the other hand what is left corresponds to a product of free-particle probability amplitudes which is analytically known. In fact, for a single probability amplitude

$$\langle \vec{q}_{N-1}|(e^{-i\hat{T}\Delta t/\hbar}e^{-i\hat{V}\Delta t/\hbar})|\vec{q}_{N-2}\rangle = e^{-i\frac{V(\vec{q}_{N-1})+V(\vec{q}_{N-2})}{2}\Delta t/\hbar}\langle \vec{q}_{N-1}|e^{-i\hat{T}\Delta t/\hbar}|\vec{q}_{N-2}\rangle. \tag{19.11}$$

Eventually, Feynman derived the following expression for the coordinate representation of the quantum propagator of a system of mass m (in the first sum $q_N = q'$)

$$\begin{aligned}\langle \vec{q}'|e^{-i\hat{H}t/\hbar}|\vec{q}_0\rangle &= \lim_{N\to\infty}\left(\frac{m}{2\pi i\hbar\Delta t}\right)^{N/2}\int_{-\infty}^{+\infty} d\vec{q}_1 \ldots \int_{-\infty}^{+\infty} d\vec{q}_{N-1} \\ &\exp\left[\frac{im\Delta t}{2\hbar}\sum_{K=1}^{N}\left(\frac{q_K - q_{K-1}}{\Delta t}\right)^2\right] exp\left[-\frac{i\Delta t}{\hbar}\left(\frac{V(\vec{q}_0)}{2} + \frac{V(\vec{q}')}{2} + \sum_{k=1}^{N-1} V(\vec{q}_K)\right)\right] \\ &= \int \mathcal{D}[\vec{q}(t)]e^{iS_t(\vec{q}',\vec{q}_0)/\hbar}\end{aligned} \tag{19.12}$$

$S_t(\vec{q}', \vec{q}_0)$ is the action along the path going from $\vec{q}_0$ to $\vec{q}'$ in time t. It is defined as the time integral of the difference between kinetic and potential energies. $\int \mathcal{D}[\vec{q}(t)]$ is a special functional measure proportional to the product $\prod_{i=1}^{N-1}\int_{-\infty}^{+\infty} d\vec{q}_i$. In Figure 19.1 the integration of Eq. (19.12) is pictorially represented, with the time interval on the x-axis and the dashed vertical lines which are examples of time slices. Composition of all possible $\vec{q}_\alpha$ values at each time slice accounts for all possible path integrations.

Some of the possible paths are reported as continuous lines in Figure 19.1. Paths can be of any type, including polygonal chains (red curves). In general, they are not classical paths. Identification of all possible paths is, however, a formidable task which needs to be eased by approximating Eq. (19.12) in an appropriate way.

A stationary phase approximation [7] to the quantum propagator leads to what is called the semiclassical propagator. In detail, the stationary phase approximation to an oscillatory 1-dimensional integral can be written as

$$\int_{-\infty}^{+\infty} dx\, e^{if(x)} \approx \sum_{\{x_j | df(x_j)/dx=0\}} \sqrt{\frac{2\pi i}{d^2 f(x_j)/dx^2}}\, e^{if(x_j)}. \tag{19.13}$$

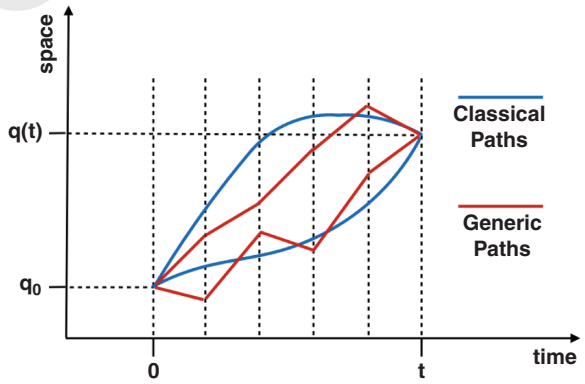

Figure 19.1 Pictorial representation of the Feynman path integral integration.

Easy extension to the multi-dimensional case is obtained by substituting $d^2f(x_j)/dx^2$ with the corresponding determinant of the matrix of second derivatives of f with respect to the position (i.e., the Hessian). This anticipates that in a SC simulation Hessian calculations are required along the trajectory. From classical mechanics it is known (Hamilton's principle) that for classical paths the functional derivative of the action with respect to a given path $\vec{q}(t)$ is zero. This is exactly the stationary phase condition for the path integral. Thus, the stationary phase approximation to the Feynman probability amplitude between $\vec{q}_0$ and $\vec{q}'$ in Eq. (19.12) leads to the following sum over all possible classical paths (called roots) connecting points $\vec{q}_0$ and $\vec{q}'$ in time t including fluctuations up to the second order around the classical action of each path

$$\langle \vec{q}' | e^{-\mathrm{i}\hat{H}t/\hbar} | \vec{q}_0 \rangle \propto \sum_{roots} e^{\mathrm{i}\left(S_t^{\mathrm{cl}}(\vec{q}',\vec{q}_0)+\frac{\partial}{\partial \vec{q}(t)}S_t^{\mathrm{cl}}(\vec{q}',\vec{q}_0)+\frac{\partial^2}{\partial \vec{q}(t)^2}S_t^{\mathrm{cl}}(\vec{q}',\vec{q}_0)\right)/\hbar}, \tag{19.14}$$

where $\partial S_t^{\mathrm{cl}}(\vec{q}',\vec{q}_0)/\partial \vec{q}(t) = 0$ because the sum is over classical paths. This is pictorially represented by the blue lines in Figure 19.1. Finding all the roots is not a trivial problem, which is generally known as the "double boundary problem". A suitable technique to overcome this formidable issue will be presented in the next section.

In the following we proceed with the algebra to determine explicitly an analytical formula for the coordinate representation of the semiclassical propagator. For simplicity we work in single dimensionality, but formulae are easily generalizable to multiple dimensions. The Feynman path integral is

$$\langle q' | e^{-\mathrm{i}\hat{H}t/\hbar} | q_0 \rangle = \lim_{N\to\infty} \left(\frac{Nm}{2\pi \mathrm{i}\hbar t}\right)^{N/2} \int_{-\infty}^{+\infty} dq_{N-1} \cdots \int_{-\infty}^{+\infty} dq_1 e^{\mathrm{i}S_N(q)/\hbar}, \tag{19.15}$$

with $(q_N = q')$ and

$$S_N(q) = \frac{Nm}{2t}\sum_{K=1}^{N}(q_K - q_{K-1})^2 - \frac{t}{N}\left[\sum_{K=1}^{N-1} V(q_K) + \frac{1}{2}(V(q_0)+V(q_N))\right]. \tag{19.16}$$

The stationary phase condition is $\partial S_N/\partial q_K = 0$ for $K = 1, N-1$ leading to the following relation for each q_K

$$-V'(q_K) = m\frac{q_{K+1}+q_{K-1}-2q_K}{\Delta t^2} \approx m\ddot{q}_K, \tag{19.17}$$

where the second derivative of the position is approximated with a central finite difference formula. Equation (19.17) is nothing other than Newton's law for the classical motion of a particle of mass m moving in the potential V, thus confirming that application of the stationary phase condition restricts the general Feynman paths to classical trajectories only. To perform the stationary phase integration (see Eq. (19.13)), upon insertion of Eq. (19.16) into Eq. (19.15) one integrates the Gaussian integrals of each path fluctuation. By writing [11]

$$\left|\frac{\partial^2 S_N}{\partial q_i \partial q_j}\right|^{-1} = -\left(\frac{t}{Nm}\right)^N \left|\frac{\partial^2 S_N}{\partial q_0 \partial q_N}\right|, \tag{19.18}$$

the final, multidimensional expression is

$$\begin{aligned}\left\langle \vec{q}' \left| e^{-\frac{\mathrm{i}}{\hbar}\hat{H}t} \right| \vec{q}_0 \right\rangle &\approx \sum_{roots}\left[-\frac{\left|\frac{\partial^2 S_t}{\partial \vec{q}' \partial \vec{q}_0}\right|}{(2\pi\mathrm{i}\hbar)^F}\right]^{1/2} \frac{e^{\frac{\mathrm{i}}{\hbar}S_t(\vec{q}',\vec{q}_0)}}{e^{\mathrm{i}\upsilon\pi/2}} \\ &= \sum_{roots}\left[(2\pi\mathrm{i}\hbar)^F \left|\frac{\partial \vec{q}'}{\partial \vec{p}_0}\right|\right]^{-1/2} \frac{e^{\frac{\mathrm{i}}{\hbar}S_t(\vec{q}',\vec{q}_0)}}{e^{\mathrm{i}\upsilon\pi/2}}\end{aligned} \tag{19.19}$$

where we have introduced the formula valid for classical trajectories $\partial S_t(\vec{q}', \vec{q}_0)/\partial \vec{q}_0 = -\vec{p}_0$ and F indicates the number of degrees of freedom [12, 13]. In Eq. (19.19) the sum is only over classical trajectories.

Equation (19.19) represents the semiclassical approximation to Feynman's path integral [7], an expression analogous to the one proposed by van Vleck many years before [13]. The exponential term $e^{-i\upsilon\pi/2}$ ensures the continuity of the complex square root of the pre-exponential factor and υ is called the Maslov index [14]. It is important to stress that the semiclassical approximation is not simply a sum over all possible classical paths of the exact Feynman path integral, but each path takes into account the second-order fluctuations around the classical path. In other words, the semiclassical approximation is able to reproduce quantum effects with high accuracy because it does not only include the interference effects generated by the sum of many classical trajectories weighted by the complex quantity $\exp[iS(\vec{q}', \vec{q}_0)/\hbar]$, but it also reproduces the quantum fluctuations $\partial^2 S_t/\partial \vec{q}' \partial \vec{q}_0$ up to the second order around each path.

19.3 The Semiclassical Initial Value Representation and the Heller–Herman–Kluk–Kay Formulation

Equation (19.19) has the intriguing feature of reproducing quantum effects starting from classical trajectories, but nevertheless its application has been quite limited. The reason for this limitation is twofold.

First, simulations are hindered by the presence of caustic points (defined by the relation $\partial \vec{q}'/\partial \vec{p}_0 = 0$) at which the determinant in the pre-exponential factor becomes singular. $\vec{q}'$ is a caustic (or focal) point for the classical trajectories started at $\vec{q}_0$ when the trajectories reach $\vec{q}'$ independently of their initial momentum. As an example, we calculate the caustic points of a 1-dimensional harmonic oscillator of unitary mass that starts at (p_0, q_0). After an evolution time T

$$q(T) = q_0 cos(\omega T) + \frac{p_0}{\omega} sin(\omega T). \tag{19.20}$$

The condition for caustic points $\partial q(T)/\partial p_0 = 0$ is in this case equivalent to $sin(\omega T)/\omega = 0$. This means that at times $T = n\pi/\omega$ the trajectory lands on the caustic points, which are located at $\pm q_0$, i.e., the inversion points of the harmonic oscillator if no momentum is given initially.

Secondly, a search for multidimensional trajectories satisfying the double boundary condition is requested.

Even though the first of the two issues can be removed analytically by means of "uniformization" approximations, which consist in switching to appropriate, caustic-free representations in proximity of the singularity, solving the double boundary problem is quite a cumbersome task in spite of the ever increasing availability of computational power.

To overcome both issues, William H. Miller incorporated an initial value representation (IVR) into the SC approximation [15]. In semiclassical IVR (SCIVR) the sum over all possible boundary-ended classical trajectories is replaced by an integration over initial momenta, such that the final position is equal to $\vec{q}'$

$$\sum_{\text{roots}} \rightarrow \int d\vec{p}_0 \left| \frac{\partial \vec{q}'}{\partial \vec{p}_0} \right| \delta(\vec{q}_t - \vec{q}'). \tag{19.21}$$

In Eq. (19.21) the determinant is the Jacobian for the change of variables from $\vec{q}'$ (the final position) to $\vec{p}_0$ (the starting momentum), while the delta function enforces the desired boundary condition.

This change of variables presents two advantages. First, the pre-exponential singularity is removed and the semiclassical approximation is uniform. Secondly, the root search is replaced by a phase space integration, which can be evaluated by means of Monte Carlo techniques with much less computational effort. Eventually, the SCIVR version of Eq. (19.19) is

$$\left\langle \vec{q}' \left| e^{-\frac{\mathrm{i}}{\hbar}\hat{H}t} \right| \vec{q}_0 \right\rangle \approx \int d\vec{p}_0 \delta(\vec{q}_t - \vec{q}') \left[\frac{|\partial \vec{q}'/\partial \vec{p}_0|}{(2\pi \mathrm{i}\hbar)^F} \right]^{1/2} \frac{e^{\frac{\mathrm{i}}{\hbar} S_t(\vec{p}_0, \vec{q}_0)}}{e^{\mathrm{i}\nu\pi/2}}. \tag{19.22}$$

For numerical calculations, the Dirac delta in Eq. (19.22) can be conveniently represented as an appropriately narrowed Gaussian function.

However, the SCIVR probability amplitude is not employed *per se*, but rather for calculating physical observables. We will use it for spectroscopic calculations using the time-dependent approach of Eq. (19.3). By inserting twice the $\vec{q}$-space identity and by means of the SCIVR probability amplitude of Eq. (19.22), the survival amplitude becomes

$$\begin{aligned} \left\langle \Xi \left| e^{-\frac{\mathrm{i}}{\hbar}\hat{H}t} \right| \Xi \right\rangle &= \int d\vec{q}' d\vec{q}_0 \langle \Xi | \vec{q}' \rangle \left\langle \vec{q}' | e^{-\frac{\mathrm{i}}{\hbar}\hat{H}t} | \vec{q}_0 \right\rangle \langle \vec{q}_0 | \Xi \rangle \\ &\approx \int d\vec{p}_0 \int d\vec{q}_0 \left[\frac{1}{(2\pi \mathrm{i}\hbar)^F} \left| \frac{\partial \vec{q}_t}{\partial \vec{p}_0} \right| \right]^{1/2} \frac{e^{\frac{\mathrm{i}}{\hbar} S_t(\vec{p}_0, \vec{q}_0)}}{e^{\mathrm{i}\nu\pi/2}} \Xi^*(\vec{q}_t) \Xi(\vec{q}_0). \end{aligned} \tag{19.23}$$

As anticipated, the great advantage of Eq. (19.23) is that now the survival probability can be evaluated via Monte Carlo integration. Calculations aimed at vibrational spectroscopy are commonly performed in normal mode coordinates. By diagonalizing the Hessian matrix at the equilibrium geometry the normal frequencies of vibrations are obtained, and the associated eigenvectors serve to define the transformation matrix from normal modes to Cartesian coordinates.

Further advances in SC dynamics were introduced by Heller [16], who inspired later work by Herman and Kluk [17], and eventually Kay [18–20]. They represented the semiclassical propagator in terms of coherent states. Coherent states ($|\vec{p}, \vec{q}\rangle$) have a Gaussian representation in coordinate space

$$\langle \vec{x} | \vec{p}, \vec{q} \rangle = \left(\frac{\det(\Gamma)}{\pi^F} \right)^{1/4} e^{-(\vec{x}-\vec{q})^{\mathrm{T}} \frac{\Gamma}{2} (\vec{x}-\vec{q}) + \mathrm{i}\vec{p}^{\,\mathrm{T}} (\vec{x}-\vec{q})/\hbar}, \tag{19.24}$$

where the Gaussian width is determined by the (usually diagonal) Γ width parameter matrix. It is possible either to reformulate the Feynman paths directly in terms of coherent states [21, 22], or to represent Eq. (19.23) on the basis of coherent states [17]. In both instances the following expression for the survival amplitude is derived

$$\begin{aligned} \left\langle \Xi \left| e^{-\frac{\mathrm{i}}{\hbar}\hat{H}t} \right| \Xi \right\rangle \approx \frac{1}{(2\pi\hbar)^F} \iint d\vec{q}_0 d\vec{p}_0 C_t(\vec{p}_0, \vec{q}_0) e^{\frac{\mathrm{i}}{\hbar} S_t(\vec{p}_0, \vec{q}_0)} \\ \times \langle \Xi | \vec{p}_t, \vec{q}_t \rangle \langle \vec{p}_0, \vec{q}_0 | \Xi \rangle, \end{aligned} \tag{19.25}$$

where, in its most general form [18],

$$C_t(\vec{p}_0, \vec{q}_0) = \sqrt{\left| \frac{1}{2} \left(\frac{\partial \vec{q}_t}{\partial \vec{q}_0} + \Gamma^{-1} \frac{\partial \vec{p}_t}{\partial \vec{p}_0} \Gamma - \mathrm{i}\hbar \frac{\partial \vec{q}_t}{\partial \vec{p}_0} \Gamma + \frac{\mathrm{i}\Gamma^{-1}}{\hbar} \frac{\partial \vec{p}_t}{\partial \vec{q}_0} \right) \right|}. \tag{19.26}$$

The semiclassical way to calculate the survival amplitude of Eq. (19.25) numerically is to perform the phase space integration by Monte Carlo methods upon sampling of the initial phase space coordinates $(\vec{p}_0, \vec{q}_0)$. The real part of the term $\langle \vec{p}_0, \vec{q}_0 | \Xi \rangle$ in Eq. (19.25) constitutes a natural weight for the Monte Carlo sampling. After the classical evolution is performed employing preferentially a

simplectic algorithm [23], at the generic time t, starting from the values of $\vec{p}_t$ and $\vec{q}_t$, the classical action $S_t(\vec{p}_0, \vec{q}_0)$ and the pre-exponential factor $C_t(\vec{p}_0, \vec{q}_0)$ are calculated. Eventually, the power spectrum is obtained by Fourier transforming Eq. (19.25)

$$I(E) = \frac{1}{2\pi\hbar}\int_{-\infty}^{+\infty} dt e^{iEt/\hbar}\frac{1}{(2\pi\hbar)^F}\iint d\vec{q}_0 d\vec{p}_0 C_t(\vec{p}_0,\vec{q}_0) \times e^{iS_t(\vec{p}_0,\vec{q}_0)/\hbar}\langle\Xi|\vec{p}_t,\vec{q}_t\rangle\langle\vec{p}_0,\vec{q}_0|\Xi\rangle. \tag{19.27}$$

19.4 A Derivation of the Heller–Herman–Kluk–Kay Propagator

Once the mathematical expression of the Heller–Herman–Kluk–Kay (HHKK) propagator has been introduced

$$(e^{-i\hat{H}t/\hbar})_{\mathrm{HHKK}} = \frac{1}{(2\pi\hbar)^F}\iint d\vec{q}_0 d\vec{p}_0 C_t(\vec{p}_0,\vec{q}_0) e^{iS_t(\vec{p}_0,\vec{q}_0)/\hbar}|\vec{p}_t,\vec{q}_t\rangle\langle\vec{p}_0,\vec{q}_0|, \tag{19.28}$$

following Miller's original derivation [24] we detail how Eq. (19.25) – and consequently Eq. (19.28) – can be derived from Eq. (19.23).

For simplicity we work in one dimension and begin by showing that an appropriate filter can be introduced into an oscillatory integral to speed up the convergence of the integration. This technique, known as Filinov filtering, is based on the insertion of a Gaussian identity into the target integral. Specifically

$$I = \int dx_0 e^{i\phi(x_0)} = \int dx_0 \int dx_G \sqrt{\frac{A}{\pi}} e^{-A(x_G-x_0)^2} e^{i\phi(x_0)}, \tag{19.29}$$

which can be approximated by expanding to the second order the function $\phi(x_0)$ around x_G and then integrating analytically in the x_0 variable

$$\begin{aligned} I &\approx \sqrt{\frac{A}{\pi}}\int dx_G \int dx_0 e^{-A(x_0-x_G)^2} e^{i[\phi(x_G)+\phi'(x_G)(x_0-x_G)+\frac{1}{2}\phi''(x_G)(x_0-x_G)^2]} \\ &= \int dx_G\, e^{i\phi(x_G)} \sqrt{\frac{A}{A-\frac{i}{2}\phi''(x_G)}}\, e^{-\phi'(x_G)^2/[4A-2i\phi''(x_G)]}. \end{aligned} \tag{19.30}$$

Equation (19.30) retains the original integrand with the addition of a damping factor that facilitates numerical convergence [25]. The A parameter can be chosen arbitrarily, but Makri and Miller suggested employing the value $A = [i\phi''(x_G) + c^{-1}]/2$, where c is a constant or a constant matrix in the multidimensional case. This choice is justified by the observation that the Gaussian identity is still approximately valid even if A is a function of the variable of integration [26].

The next step consists in applying this Filinov filter to calculate the propagation from a coherent state $|\Xi_i\rangle \equiv |p_i, q_i\rangle$ to a coherent state $|\Xi_f\rangle \equiv |p_f, q_f\rangle$ (both of Γ width) by means of van Vleck's propagator according to

$$\left\langle \Xi_f \left| e^{-\frac{i}{\hbar}\hat{H}t} \right| \Xi_i \right\rangle = \int dq_t dq_0\, (2\pi i\hbar\, \partial q_t/\partial p_0)^{-1/2}\, e^{iS_t(q_t,q_0)/\hbar}\, \langle p_f, q_f|q_t\rangle\, \langle q_0|p_i, q_i\rangle, \tag{19.31}$$

where the exponential with the Maslov index is left implicit. We work out the case of a 1-dimensional system (i.e., a bidimensional phase space) but results are generalizable to multiple dimensions. We assume also that the complex-valued pre-exponential factor in Eq. (19.31) is slowly varying with respect to the rest of the integrand, so that the filter applies only to the latter. Then, by

rearranging Eq. (19.31) in the form $I = \int dq_t\, dq_0\, A'\, e^{i\phi(q_t,q_0)}$ with A' including the pre-exponential factor and normalization constants, we need to evaluate the first and second derivatives of $\phi(q_t, q_0)$

$$\phi(q_t, q_0) = S_t(q_t, q_0) + p_i(q_0 - q_i) - p_f(q_t - q_f) + i\frac{\Gamma}{2}(q_f - q_t)^2 + i\frac{\Gamma}{2}(q_i - q_0)^2 \tag{19.32}$$

$$\frac{\partial\phi(q_t, q_0)}{\partial q_0} = -p_0 + p_i + i\Gamma(q_0 - q_i) \quad \frac{\partial\phi(q_t,q_0)}{\partial q_t} = p_t - p_f + i\Gamma(q_t - q_f) \tag{19.33}$$

$$\begin{pmatrix} \frac{\partial^2\phi(q_t,q_0)}{\partial q_t^2} & \frac{\partial^2\phi(q_t,q_0)}{\partial q_0\partial q_t} \\ \frac{\partial^2\phi(q_t,q_0)}{\partial q_t\partial q_0} & \frac{\partial^2\phi(q_t,q_0)}{\partial q_0^2} \end{pmatrix} = \begin{pmatrix} \frac{\partial p_t}{\partial q_t} + i\Gamma & \frac{\partial p_t}{\partial q_0} \\ -\frac{\partial p_0}{\partial q_t} & -\frac{\partial p_0}{\partial q_0} + i\Gamma \end{pmatrix}, \tag{19.34}$$

and then choose a diagonal Filinov parameter matrix

$$c = \begin{pmatrix} c_0 & 0 \\ 0 & c_1 \end{pmatrix}. \tag{19.35}$$

In agreement with Eq. (19.30) the Filinov filtered version of the integral in Eq. (19.31) becomes

$$I \approx \int dq_t dq_0 \left(\frac{\Gamma}{\pi}\right)^{1/2} \left(2\pi i\hbar\frac{\partial q_t}{\partial p_0}\right)^{-1/2} det[1 + ic\phi'']^{1/2}\, e^{[-\phi'^T\frac{c}{2}\phi' + i\phi]}, \tag{19.36}$$

where ϕ' is shorthand for the vector of first derivatives (Eq. (19.33)) and ϕ'' for the matrix of second derivatives in Eq. (19.34). Eventually, moving to the IVR framework

$$I \approx (2\pi\hbar)^{-1} \int dp_0 dq_0 \left(-2i\hbar\Gamma\frac{\partial q_t}{\partial p_0}\right)^{1/2} C_{\text{Fil}}\, e^{[i\phi + \phi_{\text{Fil}}]}. \tag{19.37}$$

Matrix–matrix and matrix–vector products appearing in Eq. (19.36) can be evaluated using standard algebraic manipulations. This leads to

$$C_{\text{Fil}}^2 = (1 - c_0\Gamma)(1 - c_1\Gamma) + \left(\frac{\partial q_t}{\partial p_0}\right)^{-1} \left(ic_1\frac{\partial q_t}{\partial q_0}(1 - c_0\Gamma) + ic_0(1 - c_1\Gamma)\frac{\partial p_t}{\partial p_0} - c_0c_1\frac{\partial p_t}{\partial q_0}\right)$$

$$\phi_{\text{Fil}} = -\frac{c_1}{2}[(p_t - p_f)^2 + 2i\Gamma(p_t - p_f)(q_t - q_f) - \Gamma^2(q_t - q_f)^2]$$
$$-\frac{c_0}{2}[(p_0 - p_i)^2 + 2i\Gamma(p_i - p_0)(q_0 - q_i) - \Gamma^2(q_0 - q_i)^2],$$

and the HHKK propagator of Eq. (19.28) in the mono-dimensional case is obtained by choosing $c_0 = c_1 = 1/2\Gamma$. This demonstrates that the more practical HHKK propagator can be derived as an approximate version of the van Vleck one. The key advantages of the former lie in the built-in Gaussian probability density for Monte Carlo integration and in the possibility to preserve the unitarity of the propagator longer in time thanks to its pre-exponential factor [27].

19.5 The Time-Averaging Filter

Application of the original HHKK propagator is limited to low-dimensional systems due to the presence of the oscillatory exponential in the integrand. Several methods such as cellular dynamics [28–30], Filinov and generalized Filinov filtering [26, 31, 32] have been proposed and can be effective to speed up the convergence of the Monte Carlo integration of Eq. (19.27). Here we describe in

detail a different approach based on the insertion of a time-averaging (TA) filter. Time-averaging was introduced by Elran and Kay [33, 34], and later by Kaledin and Miller [35, 36]. The idea is that starting from a phase space average of the form of the HHKK propagator

$$I_{\mathrm{PS}} = \iint d\vec{p}_0 d\vec{q}_0 A(\vec{p}_0, \vec{q}_0), \tag{19.38}$$

one can speed up convergence by time-averaging the integrand, thus damping disadvantageous oscillations. In practice, the time averaged version of I_{PS} is

$$I_{\mathrm{PS\text{-}TA}} = \iint d\vec{p}_0 d\vec{q}_0 \frac{1}{T}\int_0^T dt\, A(\vec{p}_t, \vec{q}_t), \tag{19.39}$$

which is fully equivalent to I_{PS}. The demonstration is achieved first by changing the order of integrations, and then by invoking Liouville's theorem, which guarantees that the phase-space distribution function is constant along the trajectories and the change of variables $d\vec{p}_0 d\vec{q}_0 \rightarrow d\vec{p}_t d\vec{q}_t$ has a unitary Jacobian.

$$\begin{aligned} I_{\mathrm{PS\text{-}TA}} &= \frac{1}{T}\int_0^T dt \iint d\vec{p}_0 d\vec{q}_0 A(\vec{p}_t, \vec{q}_t) \\ &= \frac{1}{T}\int_0^T dt \iint d\vec{p}_t d\vec{q}_t A(\vec{p}_t, \vec{q}_t) \\ &= \frac{1}{T}\int_0^T dt I_{PS} = I_{PS} \end{aligned} \tag{19.40}$$

The phase-space and time integrations commute, but Eq. (19.40) is exact only when, within numerical accuracy, both integrations have converged. Kaledin and Miller [35, 36] worked out the following time averaged version of Eq. (19.27)

$$\begin{aligned} I(E) = \frac{1}{(2\pi\hbar)^F} \iint d\vec{q}_0 d\vec{p}_0 \frac{1}{T}\int_0^T dt_1 \frac{Re}{\pi\hbar}\int_0^{+\infty} dt e^{\mathrm{i}Et/\hbar} \\ \times C_{t_1+t}(\vec{p}_{t_1}, \vec{q}_{t_1}) e^{\mathrm{i}S_{t_1+t}(\vec{p}_{t_1}, \vec{q}_{t_1})/\hbar} \langle \Xi | \vec{p}_{t_1+t}, \vec{q}_{t_1+t} \rangle \langle \vec{p}_{t_1}, \vec{q}_{t_1} | \Xi \rangle. \end{aligned} \tag{19.41}$$

Finally, moving from the integration variable t to $t_2 = t_1 + t$, Eq. (19.41) becomes

$$\begin{aligned} I(E) = \frac{1}{(2\pi\hbar)^F} \iint d\vec{q}_0 d\vec{p}_0 \frac{Re}{\pi\hbar T}\int_0^T dt_1 \\ \times \int_{t_1}^{+\infty} dt_2 e^{\frac{\mathrm{i}}{\hbar}(S_{t_2}(\vec{p}_0, \vec{q}_0) + Et_2)} \langle \chi | \vec{p}_{t_2}, \vec{q}_{t_2} \rangle e^{-\frac{\mathrm{i}}{\hbar}(S_{t_1}(\vec{p}_0, \vec{q}_0) + Et_1)} \\ \times \langle \vec{p}_{t_1}, \vec{q}_{t_1} | \chi \rangle C_{t_2}(\vec{p}_{t_1}, \vec{q}_{t_1}) \end{aligned} \tag{19.42}$$

which is the time-averaged SCIVR (TA-SCIVR) formula for power spectrum calculations.

We now focus on the bound states and consider a number N_{vib} of vibrational degrees of freedom. In order to get to a simpler form of Eq. (19.42), we approximate the pre-exponential factor $C_{t_2}(\vec{p}_{t_1}, \vec{q}_{t_1})$ in Eq. (19.42), in agreement with previous work [36]. We note that for the harmonic oscillator $C_{t_2}(\vec{p}_{t_1}, \vec{q}_{t_1}) = e^{-\mathrm{i}(\hbar\omega)(t_2 - t_1)/2\hbar} = e^{-\mathrm{i}(\phi(t_1) - \phi(t_2))/\hbar}$, which is a complex number of unit modulus with a time-dependent phase. The pre-exponential factor is analytically separable, i.e., $C_{t_2}(\vec{p}_{t_1}, \vec{q}_{t_1}) = C_{t_2}(\vec{p}_{t_0}, \vec{q}_{t_0}) C^*_{t_1}(\vec{p}_{t_0}, \vec{q}_{t_0})$, where $C_t(\vec{p}_0, \vec{q}_0) \approx e^{\mathrm{i}\phi(t)/\hbar}$. Inspired by this consideration, we decide to approximate for any bound degree of freedom the exact Herman Kluk prefactor to an element of unitary norm dependent on the prefactor phase $C_t(\vec{p}_0, \vec{q}_0) \approx e^{\mathrm{i}\phi(t)/\hbar}$, where $\phi(t) = \mathrm{phase}[C_t(\vec{p}_0, \vec{q}_0)]$, as suggested in Ref. [36]. Finally, noting that the integration over t_2 is for

practical purposes limited to the simulation time T and duplicating the integral by integrating from 0 to T also in t_2 (and consequently dividing the result by a factor of 2), the power spectrum formula obtained by means of this separable approximation is

$$I(E) = \left(\frac{1}{2\pi\hbar}\right)^{N_{vib}} \iint d\vec{p}_0 d\vec{q}_0 \frac{1}{2\pi\hbar T} \times \left| \int_0^T dt e^{\frac{i}{\hbar}[S_t(\vec{p}_0,\vec{q}_0)+Et+\phi_t]} \langle \Xi | \vec{p}_t \vec{q}_t \rangle \right|^2 . \quad (19.43)$$

Equation (19.43) is the "separable" version of TA SCIVR. For the phase-space integration in Eq. (19.43) the quantity $|\langle \vec{p}_0, \vec{q}_0 | \Xi \rangle|^2$ is often employed as Monte Carlo importance sampling density and named "Husimi distribution", if the reference state $|\Xi\rangle$ is chosen to be a coherent state. The choice of this Gaussian sampling density is, however, arbitrary and it can be tuned by varying the Gaussian width. The convergence issue in TA SCIVR is much alleviated since a number of trajectories of the order of just 1000 per degree of freedom is generally required, and the approach has permitted evaluation of vibrational frequencies accurately for a set of small isolated molecules including water, formaldehyde, and methane [37]. For such molecules pure quantum dynamical calculations have been also performed, so the challenge for semiclassical dynamics is to investigate much larger systems. However, for this purpose it is necessary to develop the semiclassical theory further in order to obtain reliable results on the basis of just a handful of classical trajectories.

19.6 The Multiple Coherent States SCIVR

The time-averaged version of the semiclassical propagator has permitted the first semiclassical vibrational spectroscopy calculations on real molecular systems for which high-level potential energy surfaces (PES) are available. However, the approach is strongly limited by the necessity to rely on precise, but fast-to-compute, versions of the potential. For large molecular and supra-molecular systems analytical potentials are usually not available because of the difficulty to fit an analytical expression to such large systems, or, in case a force field exists, it may be not accurate enough for reliable spectroscopic calculations. A way to overcome this PES issue is to employ ab initio on-the-fly (i.e., direct) molecular dynamics simulations, in which the potential energy and gradient calls are performed at each time step while the dynamics is in progress [38]. These simulations are very computationally demanding though, and the number of trajectories required, even by a time averaged semiclassical simulation, is too large and not affordable.

Nevertheless, ab initio on-the-fly semiclassical spectroscopy has become possible by the recent introduction of the multiple coherent (MC) technique [39]. The foundation of MC SCIVR lies in pioneering work by De Leon and Heller [40] who demonstrated on low-dimensional model systems that accurate semiclassical eigenenergies and eigenfunctions can be obtained even by means of a single trajectory if it is run at the correct (quantum) energy. MC SCIVR assumes that reliable frequency estimates can be secured also for real molecular systems if a single trajectory is employed with an energy in the neighborhood of the true (but unknown) quantum one. A straightforward way to accomplish this goal is to work in normal mode coordinates by starting the trajectory from the equilibrium molecular geometry ($\vec{q}_{\text{eq}}$) with momenta selected according to a harmonic approximation, i.e., $\vec{p}_{\text{eq}} = \sqrt{(2\vec{n}+1)\hbar\vec{\omega}}$. Another pillar on which MC SCIVR is based concerns the choice of the reference state $|\Xi\rangle$. In order to enhance the Fourier transform signal of the vibrational mode of

interest, the reference state is chosen as a coherent state centered at the phase-space point $(\vec{p}_{\rm eq}, \vec{q}_{\rm eq})$ from which the classical trajectory has originated. In general, one different trajectory per each of the N_{st} states to be investigated is run. For each state (K), the corresponding reference state $|\Xi^{(K)}\rangle$ is appropriately chosen as

$$|\Xi^{(K)}\rangle = \prod_{J=1}^{N_{vib}} \sum_{\alpha=1}^{N_\alpha} \varepsilon_{\alpha,J}^{(K)} |\, p_{{\rm eq},\alpha,J}^{(K)},\ q_{{\rm eq},\alpha,J}^{(K)}\rangle. \quad K = 1, \ldots, N_{st}. \tag{19.44}$$

N_α is the number of coherent states and associated coefficients $\varepsilon_{\alpha,J}^{(K)}$ that are employed to enforce parity or molecular symmetry to favor detection of signals corresponding to specific mode excitations or symmetry species. The examples reported below will clarify this aspect. Equation (19.43) still serves as the working formula and, for the exact case of the harmonic oscillator, the phase-space integration is substituted by a sum over the tailored trajectories ($N_{tr} = N_{st}$) [41–43]

$$I(E) = \left(\frac{1}{2\pi\hbar}\right)^{N_{vib}} \sum_{K=1}^{N_{tr}} \frac{1}{2\pi\hbar T} \left| \int_0^T dt e^{\frac{\rm i}{\hbar}[S_t^{(K)}(\vec{p}_0{}^{(K)}, \vec{q}_0{}^{(K)}) + Et + \phi_t^{(K)}]} \langle \Xi^{(K)} | \vec{p}_t{}^{(K)} \vec{q}_t{}^{(K)} \rangle \right|^2. \tag{19.45}$$

In the general case of an anharmonic and coupled potential, the total spectrum is obtained as the convolution of the spectral features provided by each trajectory in an energy range close to the energy of the trajectory.

The water molecule serves as a representative example of the technique. There are $N_{vib} = 3$ vibrational degrees of freedom, and initially we consider simulations based on just one classical trajectory ($N_{tr} = 1$) to point out the features of a specific choice of the reference state $|\Xi\rangle$ [44]. By choosing $N_\alpha = 1$ and $|\Xi\rangle = \prod_{J=1}^{N_{vib}} \varepsilon_J |p_{{\rm eq},J}, q_{{\rm eq},J}\rangle$, the total power spectrum can be easily simulated. We introduce for shorthand notation the total vector $(\vec{\varepsilon})$ collecting the coefficients ε_J, which, in this case, is made of three elements (one per degree of freedom) all equal to 1. Figure 19.2 shows indeed the time averaged power spectrum obtained by running a single classical trajectory with harmonic zero point energy (indicated in Table 19.1 as "TA SCIVR 1traj (zpe)") and $\vec{\varepsilon} = (1;1;1)$ – semicolons separate the different degrees of freedom – on an analytical potential energy surface constructed

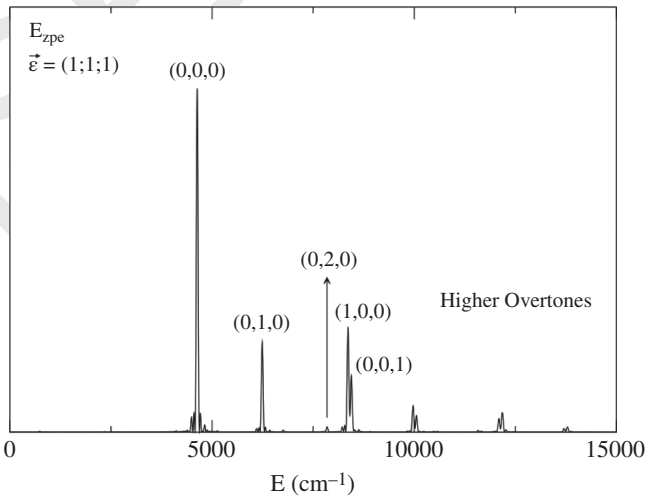

Figure 19.2 Total power spectrum of water using a single trajectory with harmonic zero point energy. Peaks are assigned and labeled by means of the usual quantum harmonic notation (symmetric stretch, bending, asymmetric stretch).

Table 19.1 Values (cm^{-1}) of zero point energy and some vibrational transitions of water. Frequency estimates are given in harmonic approximation (second column), with time averaged semiclassical dynamics based on a single trajectory with harmonic zero-point energy (third column), by means of MC SCIVR (fourth column), and quantum mechanically with a DVR technique (last column). In the last row the mean absolute error with respect to the QM values is reported. The usual quantum harmonic state notation has been employed with the first index corresponding to the symmetric stretch, the second index to the bending mode, and the third index to the asymmetric stretch.

Transition	Harm	TA SCIVR 1traj (zpe)	MC SCIVR	QM (DVR)
(0,0,0)	4711	4632	4632	4660
(0,0,0) → (0,1,0)	1650	1608	1584	1587
(0,0,0) → (0,2,0)	3300	3209	3171	3139
(0,0,0) → (1,0,0)	3830	3732	3706	3716
(0,0,0) → (0,0,1)	3941	3813	3813	3803
(0,0,0) → (1,1,0)	5480	5340	5231	5292
(0,0,0) → (0,1,1)	5591	5423	5307	5350
(0,0,0) → (2,0,0)	7660	7461	7410	7417
(0,0,0) → (0,0,2)	7882	7545	7500	7499
MAE	176	40	19	–

by Thiel et al. [45]. Due to the energetics of the trajectory, the most accurate peak is expected to be the zero-point energy (ZPE) one.

To assign peaks in the power spectrum with more confidence it is possible to insert symmetry into the calculations. This is obtained by duplicating the number of coherent states ($N_\alpha = 2$) that make up the reference state in Eq. (19.44). The dimensionality of $\vec{\varepsilon}$ is also doubled. Specifically, parity symmetry can be enforced by choosing the reference states as $|\Xi\rangle = \prod_{J=1}^{N_{vib}} (\varepsilon_{1,J} |p_{\mathrm{eq},J}, q_{\mathrm{eq},J}\rangle + \varepsilon_{2,J} |-p_{\mathrm{eq},J}, q_{\mathrm{eq},J}\rangle)$. In fact, the sign of $\varepsilon_{2,J}$ determines if an odd ($\varepsilon_{2,J} = -1$) or even ($\varepsilon_{2,J} = 1$) number of quanta in the mode J is associated to the peak to be assigned. For instance, for the ground state $\vec{\varepsilon} = (1, 1; 1, 1; 1, 1)$, while for the first excited state $\vec{\varepsilon} = (1, -1; 1, 1; 1, 1)$. This is also evident from the upper plot in Figure 19.3 where in the first of the four panels only the ZPE peak is enhanced. There are also minor peaks which can be barely seen at high energy. Some of them correspond to double excitations of the modes. In the other three panels of the same plot the first excited states of each mode have been enhanced with an appropriate choice of the ε components. All spectra were obtained from the very same single trajectory with harmonic zero point energy.

As for the molecular symmetry we note that symmetric stretch and bending of water are of a_1 symmetry, while the asymmetric stretch is of b_2 symmetry. This means that we can enforce the desired symmetry and get the corresponding peaks in the power spectrum by employing the reference state $|\Xi\rangle = \prod_{J=1}^{N_{vib}} (\lambda_{1,J} |p_{\mathrm{eq},J}, q_{\mathrm{eq},J}\rangle + \lambda_{2,J} |-p_{\mathrm{eq},J}, -q_{\mathrm{eq},J}\rangle)$. Note that the second coherent state in the linear combination is now centered at $(-p_{\mathrm{eq},J}, -q_{\mathrm{eq},J})$, and the symmetry parameters have been renamed as λ to help the reader. To discriminate between peaks, we set the value of the λ_2 component relative to the asymmetric stretch equal to 1 (a_1 symmetry) or -1 (b_2 symmetry). Figure 19.3 reports on the bottom plot the two simulations for water in which peaks are distinguished according to their molecular symmetry. The proposed methodology to enforce parity or molecular symmetry is rigorous for the harmonic oscillator but, as demonstrated by the simulations here presented, it is effective also for realistic molecular systems.

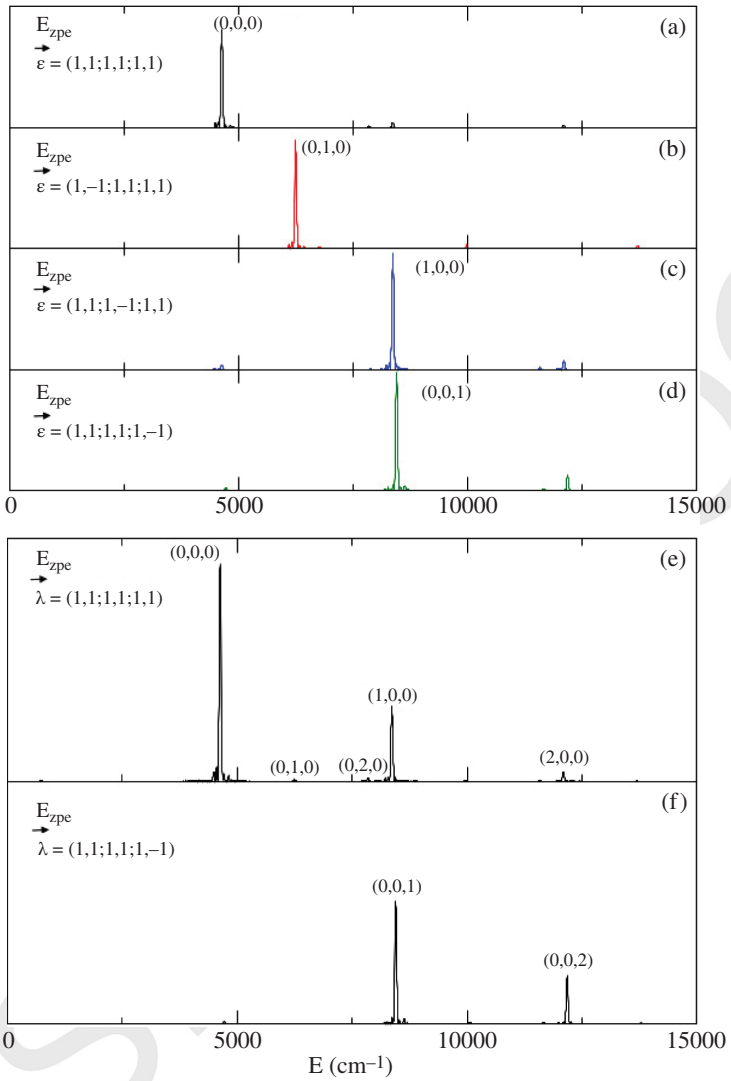

Figure 19.3 Top: Selection of water semiclassical eigenvalues from a single trajectory with harmonic zero point energy. Panel (a): zero point energy (4632 cm^{-1}, black line); panel (b): bending mode (red); panel (c): symmetric stretch (blue); panel (d): asymmetric stretch (green). Frequencies of the fundamental transitions can be obtained as differences with respect to the zero point energy. They are: $\omega_b = 1608$ cm^{-1}; $\omega_s = 3732$ cm^{-1}; $\omega_a = 3813$ cm^{-1}. Bottom: peaks are selected on the basis of molecular symmetry. On the top panel (e) modes with a_1 symmetry are presented, while the bottom panel (f) illustrates peaks with b_2 symmetry. Note that in the simulations the elements of $\vec{\varepsilon}$ and $\vec{\lambda}$ are ordered according to the ascending harmonic frequency of the modes.

So far a single harmonic zpe trajectory has been employed but, in the true spirit of the multiple coherent states technique ($N_{tr} = N_{st}$), results can be refined in a peak-by-peak fashion by running for each mode one trajectory with one quantum of excitation in that specific mode and employing the corresponding reference state. This leads to a better estimate of fundamental transition frequencies and especially overtones. Table 19.1 reports a comparison of the frequencies provided by different approaches. As expected, the enhanced accuracy of a multiple coherent technique is

evident when comparing semiclassical estimates to the quantum benchmark obtained by means of a discrete variable representation (DVR) calculation in normal mode coordinates. We stress that the simulations yield the spectrum (i.e., the eigenvalues) of the vibrational Hamiltonian, so we are able to assign a frequency even to those vibrational transitions which are not IR or Raman active.

Among remarkable applications of the MC-SCIVR method we recall a study of ammonia, which has permitted detection of the spectrum of this molecule and to mimic its peculiar tunneling splitting feature with just eight trajectories [46], and an investigation of the simplest aminoacid: glycine [47]. Glycine is characterized by several conformers as demonstrated by the multiple minimum structure of its potential energy surface. An ab initio on-the-fly MC-SCIVR approach has allowed investigation of all these conformers in full dimensionality and to estimate the potential effect of conformer interconversion on vibrational frequencies. More details on this system will be presented in Section 19.10. The advantage with respect to other methods based on calculations confined to a single well is evident. Furthermore, electronic theory calculations are needed only for the geometries experienced along the dynamics so a global full-dimensional surface (which can be very difficult to construct) is not required.

19.7 The "Divide-and-Conquer" SCIVR

Perhaps the most relevant issue that semiclassical dynamics and other quantum approaches must face is the scaling of computational overheads with the dimensionality of the system under investigation. In the case of SC approaches the challenge is to get a well resolved spectroscopic signal when the number of degrees of freedom exceeds 25–30. The principal reason for this issue is the multidimensional coherent state overlap which characterizes the SC formulation as in the case, for instance, of Eq. (19.43). In fact, a sensible signal requires all mono-dimensional coherent state overlaps to be simultaneously not negligible at each step of the dynamics, a request which is harder and harder to satisfy as the dimensionality of the problem increases. There is an evident difference with respect to classical simulations based on the Fourier transform of the dipole–dipole autocorrelation function in which a scalar product of 3-dimensional vectors is involved whatever the dimensionality of the system is.

Approaches have been developed to identify the effective vibrational modes for the calculations [48], while here we focus on the possibility to work in reduced dimensionality by projecting the full-dimensional problem onto a set of lower dimensional ones, where it is easier to have a recurring coherent state overlap. The total spectrum is eventually recollected as a convolution of the lower dimensional spectra [49]. Figure 19.4 depicts this "divide-and-conquer" (DC-SCIVR) idea. We note that the trajectory, i.e., the classical dynamics, is still performed in full dimensionality,

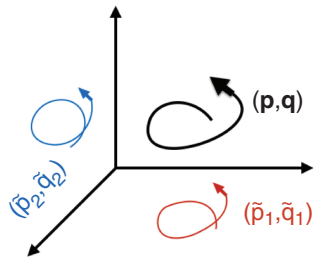

Figure 19.4 Pictorial representation of the DC-SCIVR idea. The black line is the full-dimensional trajectory while the red and blue lines represent its projection onto two different subspaces.

while associated quantities are projected onto different subspaces in which the semiclassical simulations are undertaken. The multiple coherent states reduced-dimensionality (MC-DC SCIVR) working formula becomes

$$\tilde{I}(E) = \left(\frac{1}{2\pi\hbar}\right)^{M} \sum_{K=1}^{N_{tr}} \frac{1}{2\pi\hbar T} \left| \int_0^T dt e^{\frac{i}{\hbar}[\tilde{S}_t^{(K)}(\tilde{\vec{p}}_0^{(K)}, \tilde{\vec{q}}_0^{(K)}) + Et + \tilde{\phi}_t^{(K)}]} \langle \tilde{\Xi}^{(K)} | \tilde{\vec{p}}_t^{(K)} \tilde{\vec{q}}_t^{(K)} \rangle \right|^2, \tag{19.46}$$

where M is the dimensionality of the subspace. Equation (19.46) is at the heart of the MC-DC-SCIVR approach. Mathematically, the projection process is equivalent to a singular value decomposition which allows to reduce the dimensionality of the system.

In practice, after the full-dimensional trajectory has been run, the reduced quantities appearing in Eq. (19.46) are calculated. Specifically, the prefactor phase is estimated by employing the appropriate sub-block of monodromy matrix elements, and evaluation of the coherent state overlap is straightforward. Calculation of the projected action is more complicated instead, due to the non-separability of the potential energy. In fact, if the degrees of freedom not belonging to the M-dimensional subspace are simply downgraded to parameters, then the resulting potential $V(\vec{q}(t)) \equiv V(\vec{q}_M(t); \vec{q}^{\,\mathrm{eq}}_{N_{vib}-M})$ is in general not suitable to reproduce the "correct" low-dimensional dynamics. An ideal reduced-dimensional potential should permit generation of a reduced-dimensional dynamics which, starting from the initial point in phase space $(\vec{p}_0, \vec{q}_0)$, visits all points $(\vec{p}_t, \vec{q}_t)$ obtained projecting the full-dimensional trajectory onto the subspace. This is not the case for the trivial definition proposed above. Instead, it is possible to introduce a time dependent external field

$$\begin{aligned} \tilde{V}(\vec{q}_M(t)) &= V(\vec{q}_M(t); \vec{q}^{\,\mathrm{eq}}_{N_{vib}-M}) + \lambda(t); \\ \lambda(t) &= V(\vec{q}_M(t); \vec{q}_{N_{vib}-M}(t)) - V(\vec{q}_M(t); \vec{q}^{\,\mathrm{eq}}_{N_{vib}-M}) - V(q^{\mathrm{eq}}_M; \vec{q}_{N_{vib}-M}(t)). \end{aligned} \tag{19.47}$$

This choice of the field returns the exact dynamics in the case of a separable potential, while it still provides a reliable approximation in the general instance of a non-separable potential. This means that in the DC-SCIVR simulations the projected action must be calculated by means of the potential defined in Eq. (19.47). This is achieved by performing, after the trajectory is complete, a single-energy calculation for each configuration of the dynamics upon substitution of the coordinates of the modes belonging to the subspace of interest with their equilibrium values. As usual, the transformation from normal mode coordinates to Cartesian ones is done by means of the matrix of eigenvectors of the equilibrium Hessian. The interested reader can find further details in Refs. [49–51].

Once the mathematical formalism of DC-SCIVR has been introduced, an efficient strategy to partition the full-dimensional problem into lower-dimensional ones must be devised. An educated choice of subspaces has to deal with the trade-off between simulation accuracy, which is maximum (at the net of compensation of errors) for the full-dimensional system, and the necessity to work in reduced dimensionality to get a sensible spectroscopic signal from the Fourier transform. The intuitive way to proceed consists in collecting the normal modes that are more strongly interacting into the same subspace. For this purpose a few strategies have been developed. The first one (known as the Hessian decomposition method) is based on averaging the off-diagonal elements of the normal mode Hessian matrix (which are initially 0 since the normal-mode Hessian is diagonal at the starting equilibrium geometry) dynamically along the harmonic zero-point-energy trajectory and then comparing them to an arbitrary threshold. The average Hessian elements are taken as an estimate of the coupling between the modes, so, if they are above the threshold, the two involved modes are set into the same subspace. The method has been proved effective in a number of applications [49, 50] even if it suffers from the arbitrariness of the threshold choice. In fact, if the threshold is

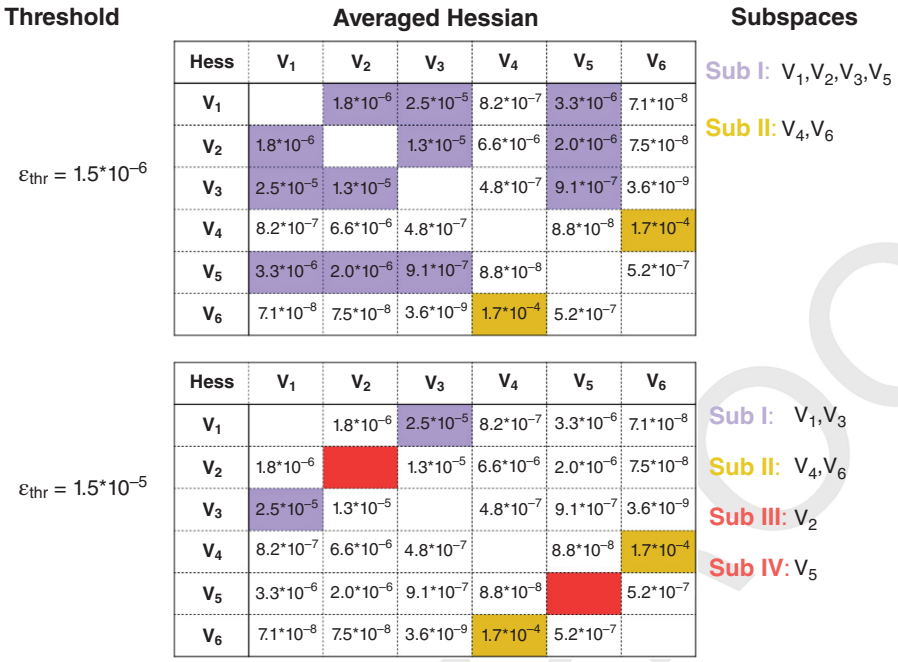

Hess	V_1	V_2	V_3	V_4	V_5	V_6
V_1		$1.8*10^{-6}$	$2.5*10^{-5}$	$8.2*10^{-7}$	$3.3*10^{-6}$	$7.1*10^{-8}$
V_2	$1.8*10^{-6}$		$1.3*10^{-5}$	$6.6*10^{-6}$	$2.0*10^{-6}$	$7.5*10^{-8}$
V_3	$2.5*10^{-5}$	$1.3*10^{-5}$		$4.8*10^{-7}$	$9.1*10^{-7}$	$3.6*10^{-9}$
V_4	$8.2*10^{-7}$	$6.6*10^{-6}$	$4.8*10^{-7}$		$8.8*10^{-8}$	$1.7*10^{-4}$
V_5	$3.3*10^{-6}$	$2.0*10^{-6}$	$9.1*10^{-7}$	$8.8*10^{-8}$		$5.2*10^{-7}$
V_6	$7.1*10^{-8}$	$7.5*10^{-8}$	$3.6*10^{-9}$	$1.7*10^{-4}$	$5.2*10^{-7}$	

Hess	V_1	V_2	V_3	V_4	V_5	V_6
V_1		$1.8*10^{-6}$	$2.5*10^{-5}$	$8.2*10^{-7}$	$3.3*10^{-6}$	$7.1*10^{-8}$
V_2	$1.8*10^{-6}$		$1.3*10^{-5}$	$6.6*10^{-6}$	$2.0*10^{-6}$	$7.5*10^{-8}$
V_3	$2.5*10^{-5}$	$1.3*10^{-5}$		$4.8*10^{-7}$	$9.1*10^{-7}$	$3.6*10^{-9}$
V_4	$8.2*10^{-7}$	$6.6*10^{-6}$	$4.8*10^{-7}$		$8.8*10^{-8}$	$1.7*10^{-4}$
V_5	$3.3*10^{-6}$	$2.0*10^{-6}$	$9.1*10^{-7}$	$8.8*10^{-8}$		$5.2*10^{-7}$
V_6	$7.1*10^{-8}$	$7.5*10^{-8}$	$3.6*10^{-9}$	$1.7*10^{-4}$	$5.2*10^{-7}$	

Figure 19.5 Influence of the choice of the threshold parameter on the partition of a 6-dimensional space into subspaces. For $\varepsilon = 1.5 \cdot 10^{-6}$ the six vibrational modes are collected into a 4-dimensional space and a 2-dimensional one. For $\varepsilon = 1.5 \cdot 10^{-5}$ there are two bi-dimensional subspaces and two mono-dimensional ones identified by a red entry in the diagonal. Diagonal Hessian elements are not of interest and they have not been reported.

too small, then the full-dimensional work space is left unchanged, whereas, if the threshold is too big, then all subspaces are inaccurately chosen to be mono-dimensional ones. Figure 19.5 exemplifies the different partition into subspaces obtained for a 6-mode model system when modifying the threshold parameter. Note that in the top panel modes ν_3 and ν_5 are in the same subspace even if they are not sufficiently coupled. This is because they are both strongly coupled to other modes (ν_1 and ν_2 in this specific case). A similar methodology, but still dependent on an arbitrary parameter, is based on an average along the trajectory of the monodromy matrix elements instead of the Hessian [48].

To make the subspace partition less arbitrary, a procedure based on the unitarity of the determinant of the phase-space Jacobian in the subspaces has been developed [50]. This approach is known as the Jacobi decomposition method. The starting point is the definition of the full dimensional Jacobian (equivalent to the monodromy matrix) as

$$\mathbf{J}(t) = \begin{pmatrix} \partial\vec{q}_t/\partial\vec{q}_0 & \partial\vec{q}_t/\partial\vec{p}_0 \\ \partial\vec{p}_t/\partial\vec{q}_0 & \partial\vec{p}_t/\partial\vec{p}_0 \end{pmatrix}, \tag{19.48}$$

whose determinant is equal to 1 at all times. This property is easy to demonstrate because at time 0 the determinant equals 1, and its time derivative is identically zero independently of time. A direct and important consequence is that $d\vec{p}_t d\vec{q}_t = d\vec{p}_0 d\vec{q}_0$, one of the ways to express Liouville's theorem of Hamiltonian mechanics. If we define a set of N_{sub} subspaces as requested by DC SCIVR, the determinant of the full-dimensional Jacobian can be calculated as the product of the partial determinants defined by the projected positions and momenta, i.e., $det(\mathbf{J}) = \prod_{i=1}^{N_{sub}} det(\tilde{\mathbf{J}}_i)$. If the

system is separable, the unitarity of the determinant is valid also in the reduced-dimensionality subspaces (i.e., $d\vec{p}_t d\vec{q}_t = d\vec{p}_0 d\vec{q}_0$) but this is no longer true for the generic case of a non-separable system. In general, the determinant of the Jacobian is not conserved in the subspaces, so a good criterion to select the best way to collect vibrational modes is one that preserves as much as possible the Jacobian determinant. For this purpose it is possible to employ an iterative procedure consisting in evaluating along the dynamics the Jacobian determinants of all possible reduced-dimensional subspaces. At each time step and for each dimensionality, the best subspace is the one with the closest Jacobian determinant to unity. Within a given dimensionality the overall best subspace is then chosen to be the one that most frequently had $det(\tilde{\mathbf{J}})$ closest to unity. Finally, the representative candidates of all subspaces of different dimensionality are compared among them and the one with the Jacobian determinant closest to unity is selected. The whole procedure is then repeated for the remaining degrees of freedom until all of them have been assigned. Figure 19.6 sketches the methodology for a 6-dimensional model system. Note that in the example a 4-dimensional subspace is selected, which means the procedure will be repeated involving only modes four and six that end

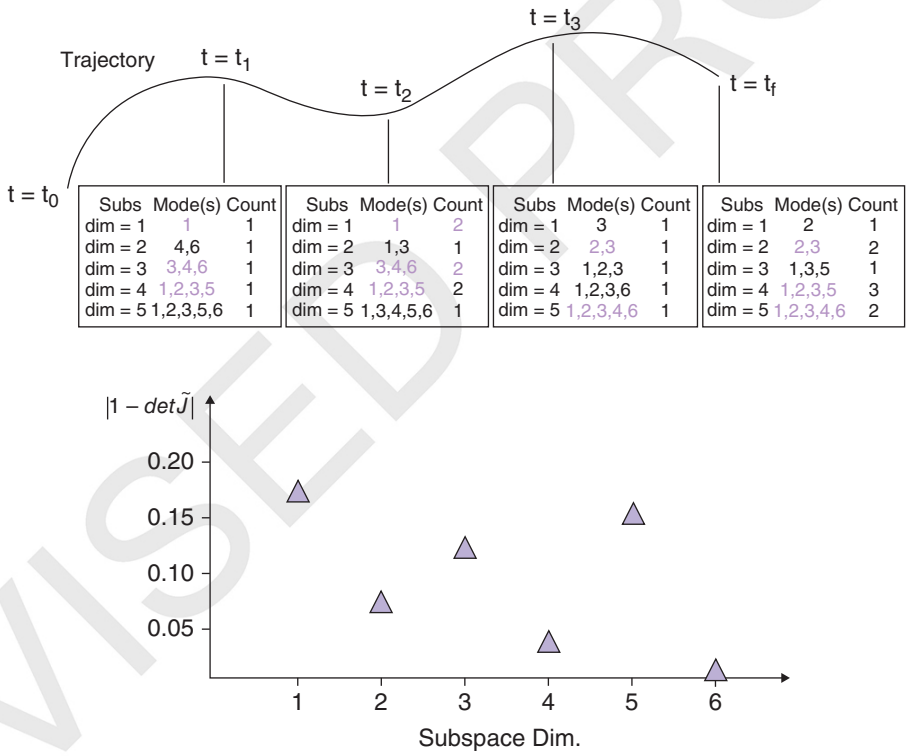

Figure 19.6 Schematic representation of the Jacobi decomposition method. First the best set of modes for each possible subspace dimensionality is calculated at every step along the trajectory. This is shown in the four boxes, where the "Subs" column indicates the subspace dimensionality and the "Count" one the incremental number of times that particular set of modes has been selected along the trajectory. For each subspace dimensionality the most frequent mode combination acts as the representative of that subspace dimensionality and it is highlighted (violet). Then, $|1 - \det\tilde{J}|$ values of all the representatives are averaged over the trajectory and compared (bottom, triangles). The 4-dimensional subspace made of modes 1,2,3,5 has the lowest $|1 - \det\tilde{J}|$ average value and it is therefore selected. Modes 4 and 6 are left and the procedure is reiterated for these two remaining degrees of freedom to check out if they belong to the same bi-dimensional subspace or if they split into a pair of mono-dimensional subspaces.

up either in a single 2-dimensional subspace or in two separate mono-dimensional subspaces. The latter instance is, in principle, not desirable but part of the interactions are anyway preserved due to the full-dimensional trajectory on which projected quantities are based. The Hessian and Jacobi decomposition methods provide generally different types of subspace partitions. On the one hand, the Jacobi approach has been shown to lead to more accurate results [50], but it is harder and harder to apply it as the total number of degrees of freedom increases due to the necessity to check all possible vibrational mode subsets. On the other hand, the Hessian decomposition approach is less accurate and depends on an arbitrary parameter, but its application is instantaneous once the averaged Hessian has been computed.

We conclude this section by reporting on an application of DC SCIVR to C_{60} fullerene, a system made of 174 vibrational degrees of freedom. A force field originally created to study graphene layers is adapted to permit analytical potential calls but, nevertheless, these are very time consuming, so a MC-DC-SCIVR approach is employed by running 175 classical trajectories about 1.2 ps long (1 at harmonic zero point energy plus other 174, each one with a harmonic quantum of excitation in a different mode). The subspaces are determined by means of the Hessian decomposition criterion based on the harmonic zero-point energy. We first scan the maximum subspace dimensionality for different values of the threshold parameter as shown in Figure 19.7, and then choose for the threshold the value $\epsilon = 10^{-6}$ corresponding to a maximum subspace dimensionality of 25. This choice is driven by the trade-off between expected accuracy and the possibility to collect a sensible spectral signal. The whole degrees of freedom are consequently collected into one

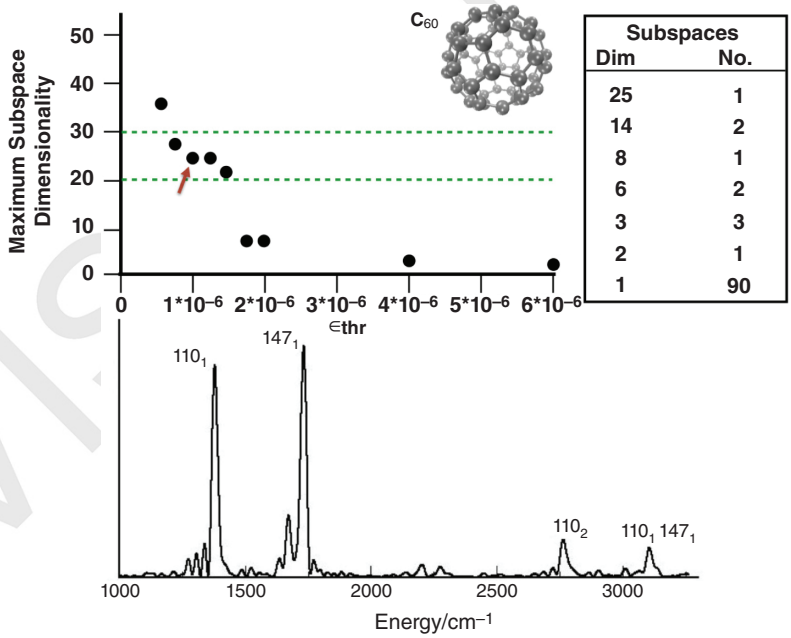

Figure 19.7 Maximum subspace dimensionality versus threshold when applying the Hessian decomposition method to the C_{60} fullerene molecule (top). The red arrow indicates the chosen threshold and the corresponding maximum subspace dimensionality. The green dashed lines determine the desired range for the maximum subspace dimensionality. The table reports the detailed partition into subspaces. On the bottom, a bi-dimensional DC-SCIVR spectrum (involving modes 110 and 147) is shown (the zpe of the subspace has been shifted to zero).

25-dimensional, two 14-dimensional, one 8-dimensional, two 6-dimensional, three 3-dimensional, one bi-dimensional, and 90 mono-dimensional subspaces.

Once the subspaces have been determined, MC-DC-SCIVR calculations can be performed. On the bottom of Figure 19.7 an example concerning a bi-dimensional subspace is reported where the two fundamentals and some overtones are clearly detected. For detailed results we refer to a previous publication (see Ref. [49]). Here we conclude this section by pointing out that even if, as already demonstrated, molecular symmetry can be incorporated into semiclassical dynamics to facilitate peak assignment, it does not help speed up calculations and it is not necessary for a good outcome of DC-SCIVR simulations, which are successful independently of symmetry.

19.8 Mixed SCIVR Dynamics: Towards Semiclassical Spectroscopy in Condensed Phase

The various semiclassical methodologies so far presented have in common the characteristic to be based on the evolution of Gaussian wave packets of fixed width. Such propagators go under the collective name of "Frozen Gaussian propagators". Another family of semiclassical Gaussian propagators has been introduced [52] in which the Gaussian width is permitted to change in time. They are called "Thawed Gaussian propagators". In practice (for simplicity we illustrate equations in one dimension, but generalization to multiple dimensions is straightforward) the wave packet is chosen to be of the coherent state form

$$\Xi(q,t) = \left(\frac{\Gamma_0}{\pi}\right)^{1/4} \exp\left[-\frac{\Gamma_t}{2}(q-q_t)^2 + \frac{\mathrm{i}}{\hbar}p_t(q-q_t) + \frac{\mathrm{i}}{\hbar}\delta_t\right], \tag{19.49}$$

with the usual Hamiltonian evolution for q_t and p_t, and the appropriate equations of motions for Γ_t and δ_t

$$\begin{aligned} -\mathrm{i}\hbar\frac{d\Gamma_t}{dt} &= -\hbar^2\Gamma_t^2 + \frac{d^2V(q_t,t)}{dq_t^2} \\ \frac{d\delta_t}{dt} &= \frac{p_t^2}{2} - V(q_t,t) - \frac{\hbar^2}{2}\Gamma_t. \end{aligned} \tag{19.50}$$

Thawed Gaussian propagation is known to be less accurate than the Heller–Herman–Kluk–Kay one, but its major flexibility allows results of good accuracy to be gained with just a single Gaussian propagation.

An interesting development of semiclassical dynamics involving both Frozen and Thawed Gaussian propagators is represented by Grossmann's hybrid (or mixed) SCIVR and its recent simplified version [53]. The method is based on the observation that the Thawed Gaussian propagator can be obtained as an approximation to the HHKK one [54]. In mixed SCIVR, the higher HHKK level of theory is reserved for a few degrees of freedom, while all the others are treated by means of the computationally cheaper Thawed Gaussian propagator. A promising application of the technique is represented by the spectroscopic investigation of a molecular system embedded in an environment. In spectroscopic applications of the mixed SCIVR the starting point is the time-averaged version of the HHKK propagator in Eq. (19.43). On this propagator the mixed approximation is inserted. The total $2F$ phase-space variables are divided into $2F_{\mathrm{HHKK}}$ for the system and $2F_{\mathrm{TG}}$ for the bath. The system, on which more accurate information is sought, is represented with the HHKK label, meaning it is treated at the HHKK level of theory, whereas the environmental degrees of freedom are indicated with the subscript TG and treated by means of the Thawed Gaussian propagator. The

method, similar to DC SCIVR, is characterized by classical dynamics runs in full dimensionality. The partition of the degrees of freedom is adopted only in the semiclassical formalism. In fact, if the Gaussian reference state $|\Xi\rangle = |\vec{p}_{\rm eq}, \vec{q}_{\rm eq}\rangle$ is chosen, where $\vec{q}_{\rm eq}$ is the equilibrium position and $\vec{p}_{\rm eq}$ is the momentum corresponding to an approximate eigenenergy, then the initial phase space coordinates $(\vec{p}_0, \vec{q}_0)$ are defined as

$$\vec{p}_0 = \begin{pmatrix} \vec{p}_{\rm HHKK,0} \\ \vec{p}_{\rm eq,TG} \end{pmatrix}, \qquad \vec{q}_0 = \begin{pmatrix} \vec{q}_{\rm HHKK,0} \\ \vec{q}_{\rm eq,TG} \end{pmatrix}. \tag{19.51}$$

The HHKK initial conditions $(\vec{p}_{\rm HHKK,0}, \vec{q}_{\rm HHKK,0})$ are selected by means of the usual Monte Carlo sampling around $(\vec{p}_{\rm eq,HHKK}, \vec{q}_{\rm eq,HHKK})$, while the bath starting coordinates are always at the equilibrium positions, $(\vec{p}_{\rm TG,0}, \vec{q}_{\rm TG,0}) = (\vec{p}_{\rm eq,TG}, \vec{q}_{\rm eq,TG})$. Then, expansion of classical trajectories and action to first and second order, respectively, in the displacement coordinates of the bath subspace allows the phase-space integration over the original initial bath conditions $(\vec{p}_{\rm TG,0}, \vec{q}_{\rm TG,0})$ to be performed analytically. In this way the dimensionality of the phase space integration is reduced. Finally, by expanding all quantities to second order for the bath variables we arrive at the separable mixed TA-SCIVR (M-TA SCIVR)

$$\begin{aligned} I(E) = \frac{1}{(2\hbar)^F} \frac{1}{\pi^{F_{\rm HHKK}}} \frac{1}{2\pi\hbar T} \int {\rm d}\vec{p}_{\rm HHKK,0} \int {\rm d}\vec{q}_{\rm HHKK,0} \left| \int_0^T {\rm d}t\, {\rm e}^{{\rm i}[Et + \phi_t(\vec{p}_0,\vec{q}_0) + S_t(\vec{p}_0,\vec{q}_0)]/\hbar} \right. \\ \times \langle \vec{p}_{\rm eq,HHKK}, \vec{q}_{\rm eq,HHKK} | \vec{p}_{{\rm HHKK},t}, \vec{q}_{{\rm HHKK},t} \rangle \langle \vec{p}_{\rm eq,TG}, \vec{q}_{\rm eq,TG} | \vec{p}_{{\rm TG},t}, \vec{q}_{{\rm TG},t} \rangle \\ \left. \times \frac{1}{[\det(\mathbf{A}(t) + \mathbf{A}^*(t))]^{1/4}} \exp\left\{ \frac{1}{4} \vec{b}_t^{\,\rm T} (\mathbf{A}(t) + \mathbf{A}^*(t))^{-1} \vec{b}_t \right\} \right|^2 . \end{aligned} \tag{19.52}$$

The elements of the matrix $\mathbf{A}(t)$ are defined as

$$\begin{aligned} A_{11}(t) &= \frac{1}{4} M_{21}^{\rm T}(t)\, \mathbf{\Gamma} M_{21}(t) + \frac{1}{4\hbar^2} M_{11}^{\rm T}(t)\, \mathbf{\Gamma}^{-1} M_{11}(t) \\ A_{12}(t) &= \frac{1}{4} M_{21}^{\rm T}(t)\, \mathbf{\Gamma} M_{22}(t) + \frac{1}{4\hbar^2} M_{11}^{\rm T}(t)\, \mathbf{\Gamma}^{-1} M_{12}(t) \\ A_{21}(t) &= \frac{1}{4} M_{22}^{\rm T}(t)\, \mathbf{\Gamma} M_{21}(t) + \frac{1}{4\hbar^2} M_{12}^{\rm T}(t)\, \mathbf{\Gamma}^{-1} M_{11}(t) \\ A_{22}(t) &= \frac{1}{4} M_{22}^{\rm T}(t)\, \mathbf{\Gamma} M_{22}(t) + \frac{1}{4\hbar^2} M_{12}^{\rm T}(t)\, \mathbf{\Gamma}^{-1} M_{12}(t), \end{aligned} \tag{19.53}$$

while the vector $\vec{b}(t) \equiv (\vec{b}_{1,t}^{\,\rm T}, \vec{b}_{2,t}^{\,\rm T})^{\rm T}$ is made of the sub-vectors

$$\begin{aligned} \vec{b}_{1,t}^{\,\rm T} &= -\frac{1}{2} (\vec{q}(t) - \vec{q}(0))^{\rm T} \left[\mathbf{\Gamma} M_{21}(t) + \frac{\rm i}{\hbar} M_{11}(t) \right] \\ &\quad - \frac{1}{2\hbar^2} (\vec{p}(t) - \vec{p}(0))^{\rm T} \left[\mathbf{\Gamma}^{-1} M_{11}(t) - {\rm i}\hbar M_{21}(t) \right] \\ \vec{b}_{2,t}^{\,\rm T} &= -\frac{1}{2} (\vec{q}(t) - \vec{q}(0))^{\rm T} \left[\mathbf{\Gamma} M_{22}(t) + \frac{\rm i}{\hbar} M_{12}(t) \right] \\ &\quad - \frac{1}{2\hbar^2} (\vec{p}(t) - \vec{p}(0))^{\rm T} [\mathbf{\Gamma}^{-1} M_{12}(t) - {\rm i}\hbar M_{22}(t)], \end{aligned} \tag{19.54}$$

where $(\vec{p}(t), \vec{q}(t))$ is the trajectory starting from the initial conditions defined in Eq. (19.51). The M_{ij} in the above equations are the $F \times F_{\mathrm{TG}}$ sub-matrices of the stability matrix,

$$\begin{aligned} M_{11}(t) &= \frac{\partial \vec{p}_t}{\partial \vec{p}_{\mathrm{TG},0}}, \quad M_{12}(t) = \frac{\partial \vec{p}_t}{\partial \vec{q}_{\mathrm{TG},0}}, \\ M_{21}(t) &= \frac{\partial \vec{q}_t}{\partial \vec{p}_{\mathrm{TG},0}}, \quad M_{22}(t) = \frac{\partial \vec{q}_t}{\partial \vec{q}_{\mathrm{TG},0}}. \end{aligned} \tag{19.55}$$

In Eq. (19.52) the Monte Carlo integration involves only the system coordinates, while the bath degrees of freedom are included through the dynamics which starts from the conditions in Eq. (19.51). The interested reader will find more details in Refs. [53, 55, 56].

The mixed SC-IVR approach is effective, but, when studying systems characterized by a large number of degrees of freedom, spectra are noisy and difficult to interpret. To overcome this issue a simplified approach to M-TA SCIVR (SAM) has been introduced. It is based on two assumptions. First, the following bath components are replaced by their analytic harmonic oscillator results

$$\begin{aligned} &\frac{1}{[\det(\mathbf{A}_{\mathrm{HO}}(t) + \mathbf{A}^*_{\mathrm{HO}}(t))]^{1/4}} \approx (2\hbar)^{F_{\mathrm{TG}}/2} \\ &\vec{b}^{\,\mathrm{T}}_{t,\mathrm{HO}}(\mathbf{A}_{\mathrm{HO}}(t) + \mathbf{A}^*_{\mathrm{HO}}(t))^{-1}\vec{b}_{t,\mathrm{HO}} \approx 0, \end{aligned} \tag{19.56}$$

(where HO stands for Harmonic Oscillator) which permits Eq. (19.52) to be considerably simplified, transforming it into

$$\begin{aligned} I(E) = \frac{1}{(2\pi\hbar)^{F_{\mathrm{HHKK}}}} \frac{1}{2\pi\hbar T} \int \mathrm{d}\vec{p}_{\mathrm{HHKK},0} \int \mathrm{d}\vec{q}_{\mathrm{HHKK},0} \\ \times \left| \int_0^T \mathrm{d}t\, \mathrm{e}^{\mathrm{i}[Et + \phi_t(\vec{p}_0,\vec{q}_0) + S_t(\vec{p}_0,\vec{q}_0)]/\hbar} \langle \vec{p}_{\mathrm{eq}}, \vec{q}_{\mathrm{eq}} | \vec{p}_t, \vec{q}_t \rangle \right|^2 . \end{aligned} \tag{19.57}$$

Then, the multiple coherent technique is employed and the final SAM working formula is

$$\begin{aligned} I(E) = \frac{1}{(2\pi\hbar)^{F_{\mathrm{HHKK}}}} \frac{1}{2\pi\hbar T} \int \mathrm{d}\vec{p}_{\mathrm{HHKK},0} \int \mathrm{d}\vec{q}_{\mathrm{HHKK},0} \\ \left| \int \mathrm{d}t\, \mathrm{e}^{\mathrm{i}[Et + \phi_t(\vec{p}_0,\vec{q}_0) + S_t(\vec{p}_0,\vec{q}_0)]/\hbar} \langle \vec{p}_{\mathrm{eq,HHKK}}, \vec{q}_{\mathrm{eq,HHKK}} | \vec{p}_{\mathrm{HHKK},t}, \vec{q}_{\mathrm{HHKK},t} \rangle \right|^2 . \end{aligned} \tag{19.58}$$

It should be pointed out that, in spite of the different derivations of SAM and DC SCIVR, both methods are in fact related. Adoption of the few-trajectory approach from MC SCIVR to Eq. (19.58) by replacing the HK initial state $|\vec{p}_{\mathrm{eq,\,HHKK}}, \vec{q}_{\mathrm{eq,\,HHKK}}\rangle$ with $|\Xi\rangle$ from Eq. (19.44) turns the phase space integration into a sum over (few) trajectories. The resulting equation has the same structure as the MC-DC-SCIVR working formula of Eq. (19.46), except for the specific form of the action and the prefactor phase. In this sense, SAM can be seen as an intermediate step between HK SCIVR and DC SCIVR. A remarkable application of the method has permitted a full study of anharmonic vibrations of the iodine molecule to be performed (I_2) in a krypton matrix made of 218 atoms [56]. This shows that SAM is a promising tool for performing highly accurate condensed phase spectroscopy in the near future.

19.9 Semiclassical Spectroscopy Workflow

Before showing some applications of SC dynamics, we present a workflow chart (Figure 19.8) summarizing the steps on which the various semiclassical approaches previously described are based. This chart keeps evolving as new semiclassical methodologies are being developed.

Relevant input data for the simulations include the reference state and the number of classical trajectories to be run. A preliminary routine optimization of the equilibrium geometry and calculation of harmonic frequencies (as usual via Hessian diagonalization) are requested. Afterwards, the chart branches according to the number of trajectories chosen. On the one hand, if just a single or a few trajectories are employed, then either thawed Gaussian propagation or the family of multiple coherent approaches is enabled. In this case, initial conditions for the trajectories are tailored, and upon classical evolution and Hessian calculation the corresponding mathematical expressions are used to get the spectrum. On the other hand, when Monte Carlo phase-space integration is performed by means of thousands of trajectories, initial conditions are sampled from a distribution (generally a Husimi one). Again, after dynamics evolution and Hessian calculation, application of the appropriate equations allows us to get the spectrum. A third instance is represented by M-TA SCIVR, which employs a multiple trajectory approach for the system and a thawed Gaussian (single trajectory) approach for the bath. For the required electronic structure calculations the freely available NWChem suite of codes is suggested [57] due to its interface with VENUS. VENUS is another free software for ab initio dynamical calculations [58] which includes semiclassical codes [59].

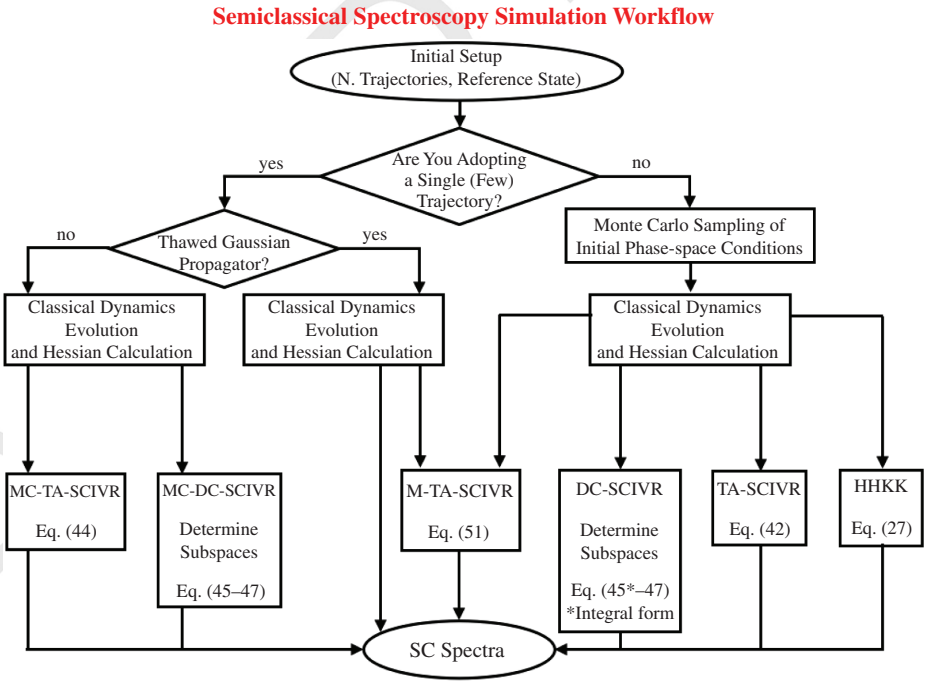

Figure 19.8 Workflow chart.

19.10 A Taste of Semiclassical Spectroscopy

A few relevant applications of semiclassical spectroscopy to molecular power, photoemission, and photoabsorption spectra are presented in this section. The semiclassical calculations of power and photoemission spectra involve electronic ground state dynamics, while photoabsorption spectra rely on electronic excited state dynamics in agreement with the formulae reported in the introductory section of the chapter.

The first application regards gas-phase glycine [47]. An analysis of the potential energy surface of this simple amino acid reveals quite a complex landscape with the presence of four conformers. Three of them are separated by small barriers which may favor conformer interconversion. The dynamics employed in the SC simulations shows that conformer interconversion takes place when exciting selectively some of the normal modes or when starting from Conf IV. This is confirmed in the top panel of Figure 19.9 by the much broader peaks obtained for Conf IV whose dynamics at harmonic zero point energy (even if less than 1 ps long) moves fast back and forth to Conf I. This aspect allows us to point out a couple of peculiar features of semiclassical dynamics. One is that the dynamics permits us to visit the effective portion of the potential energy surface and in this way construction of a global PES is not needed and ab initio on-the-fly calculations are fully legitimated. The second characteristic is that power spectra have a band shape determined by the dynamics. Results for Conf IV are corroborated by experiments performed at 13 K in argon matrices, which are much more difficult and less resolved for Conf IV [60]. The semiclassical calculations performed for glycine are based on an ab initio molecular dynamics at DFT-B3LYP level of theory with aVDZ basis set associated to MC SCIVR in full dimensionality. Results are in good agreement with experiments, and the interested reader can find all the details in Ref. [47]. Very recent work in the field has permitted calculation of the semiclassical IR spectrum of glycine [71].

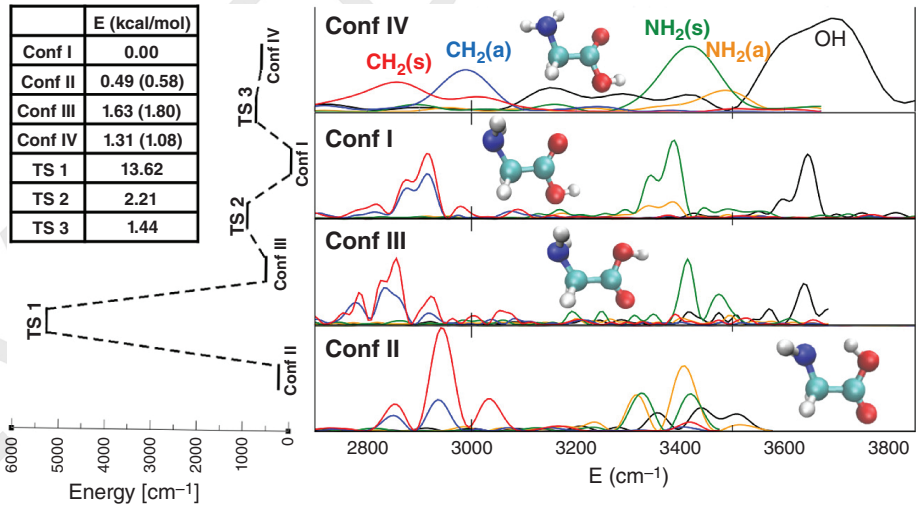

Figure 19.9 Left: Energetics of glycine calculated at DFT-B3LYP level of theory with aVDZ basis set. Energy values in parentheses include the harmonic zero-point energy contribution. Right: High frequency range vibrational power spectra for the four conformers of glycine. Peaks identify the OH (black), NH_2 asymmetric (orange), NH_2 symmetric (green), CH_2 asymmetric (blue), and CH_2 symmetric (red) stretches.

Another interesting application of semiclassical spectroscopy involving glycine is represented by the supra-molecular system made of protonated glycine tagged with hydrogen molecules. The goal is to reproduce and explain on a quantum mechanical basis the intriguing features of a recent experiment by Williams, Rizzo and coworkers [61]. In particular, in the experiment, the OH stretch signal presents twin peaks, separated by about 50 cm^{-1}, where it appears that at least three hydrogen molecules are present. The reason is that while the first pair of H_2 molecules interacts with the amino group of the protonated glycine, the third H_2 moiety can still interact either with the NH_3 group or with the hydroxyl. In this latter instance, the OH stretch is weakened and a second red-shifted peak is found in the experiment consistently with the mixture of the two conformers. Another feature of Williams and Rizzo's spectra is that the lowest in frequency among the three NH_3 bands is more and more blue-shifted as the number of tagging H_2 molecules increases, with a second peak appearing when three hydrogen molecules are involved. The blue shift is of about 60 cm^{-1}. This time the effect can be explained with a re-orientation of the NH_3 group which weakens the intramolecular hydrogen bond leading to a blue shift of the NH_3 signal. A theoretical description at the harmonic level fails even upon an ad-hoc scaling of frequencies calibrated on the OH stretch. In particular, the blue shift of the NH_3 peak is too overestimated predicting a complete cleavage of the intramolecular hydrogen bond instead of its simple weakening. This drawback is found also in a classical simulation based on the Fourier transform of the velocity–velocity correlation function. Conversely, a semiclassical description is able to gather both features, and frequencies are found within 20–30 cm^{-1} of the experiment. This SC simulation has been performed by means of the MC-DC-SCIVR technique interfaced to an ab initio on-the-fly molecular dynamics less than 1 ps long at DFT-B3LYP level of theory and with aVDZ basis set. Inclusion of dispersion corrections has been considered, but without any relevant gain in accuracy [62].

So far applications have been focused on power spectra that describe vibrational features on the ground electronic state, but semiclassical approaches can also be employed to simulate vibronic emission and absorption spectra that involve different electronic surfaces. A key example is given by the on-the-fly photoemission spectra of oligothiophenes calculated by the Vaníček group on the basis of the Fourier transform of a dipole–dipole autocorrelation function in Franck–Condon approximation (i.e., vertical electronic transition) for the initial wave packet [48]. The working formula is similar to Eq. (19.6) with the roles of the electronic ground (S_0) and excited (S_1) states interchanged, and a cubic dependence on the energy difference in front of the Fourier integration. A Thawed Gaussian approach was employed, and the emission spectrum was obtained upon short-time evolution ($\approx$ 200 fs) of the vibrational ground state of S_1 on the S_0 surface. This dynamical approach permits us to go beyond a static global harmonic approximation and to account for anharmonicities. Energy calculations and geometry optimization on the excited state surface were performed with TD-DFT, CAM-B3LYP functional and 6-31+G** basis set. The DFT level of theory was employed instead for the dynamics on the ground electronic state. Figure 19.10 reports the semiclassical photoemission spectra of a series of oligothiophenes and shows excellent agreement with the experimental results. Furthermore, in this work a strategy has been implemented to assess couplings between vibrational degrees of freedom during the dynamics, and their contribution to the spectral features. The same strategy permits us also to generate a partially uncoupled dynamics in reduced dimensionality, which may serve for application of more refined semiclassical or quantum techniques. The approach is different from DC SCIVR (which is based on a frozen instead of thawed Gaussian propagator), but it makes clear that DC SCIVR as well as the other techniques described in the chapter have the potential to also be applied successfully to the simulation of photoemission (absorption) spectra.

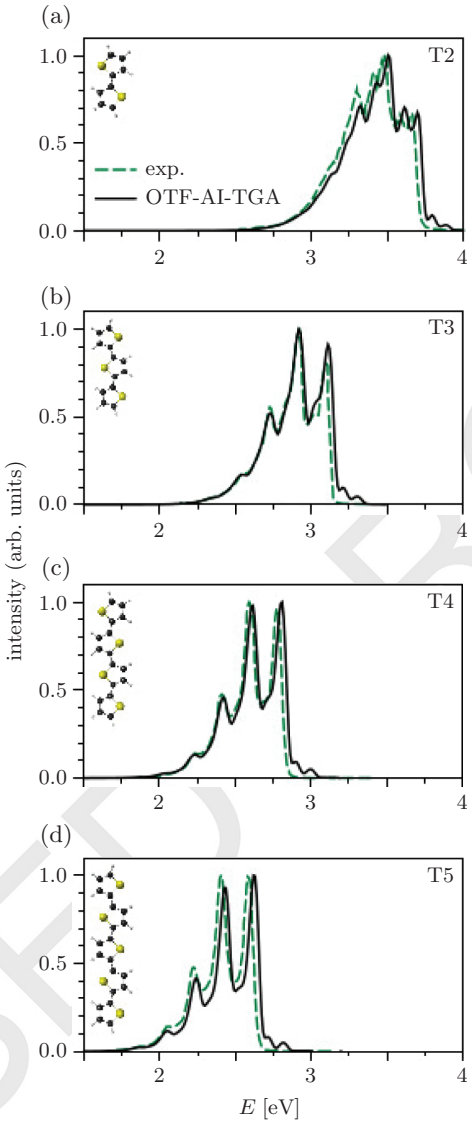

Figure 19.10 Photoemission spectra for oligothiophenes of increasing size. "OTF-AI-TGA" stands for on-the-fly ab initio thawed Gaussian approximation. Reproduced from Marius Wehrle, Miroslav Šulc, and Jiří Vaníček *The Journal of Chemical Physics* **140**, 244114 (2014), with the permission of AIP Publishing.

As a final application we consider another very recent work by the Vaníček group concerning the photoabsorption spectrum of benzene [63]. The relevant equation is Eq. (19.6), but in this case the Condon approximation cannot be invoked because the ($\tilde{A}^1\ B_{2u} \leftarrow \tilde{X}^1\ A_{1g}$) electronic transition is symmetry forbidden. However, it is vibronically allowed due to the contribution of the gradient of the transition dipole. In order to simulate the absorption spectrum of benzene one has to resort to the more refined Herzberg–Teller approximation in which the dipole depends linearly on the nuclear coordinates, i.e., $\vec{\mu}(\vec{R}) \approx \vec{\mu}(\vec{R}_{eq}) + \nabla_{\vec{R}}\vec{\mu}(\vec{R}_{eq}) \cdot (\vec{R} - \vec{R}_{eq})$. The Franck–Condon–Herzberg–Teller (FCHT) absorption spectrum of benzene (see Figure 19.11) was obtained by multiplying the initial Gaussian wave packet by a polynomial (linear) term. This

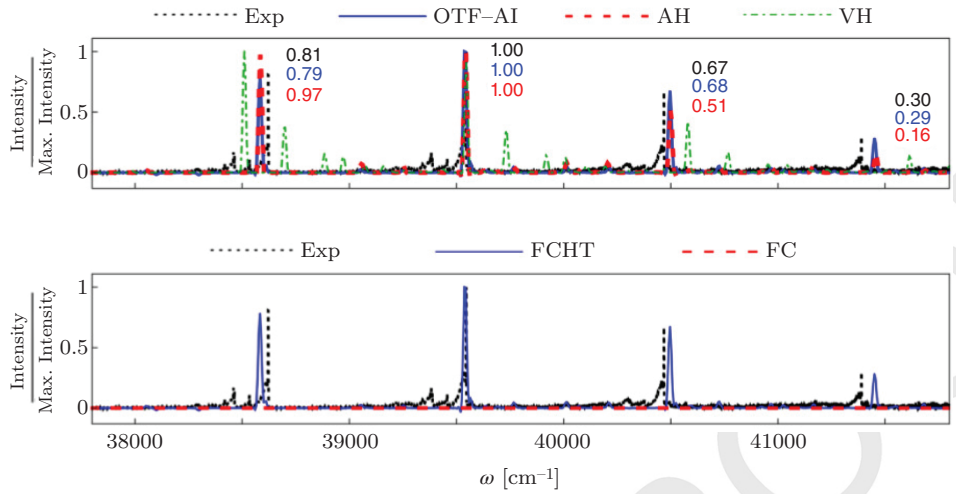

Figure 19.11 Semiclassical absorption spectra of benzene $\tilde{A}^1 B_{2u} \leftarrow \tilde{X}^1 A_{1g}$. In the top panel, a comparison between experiment and Franck–Condon–Herzberg–Teller (FCHT) spectra obtained from on-the-fly excited electronic state dynamics (OTF-AI), static adiabatic harmonic (AH), and static vertical harmonic (VH) approximations is presented. Scaled intensities are reported for each approach next to the peaks. In the bottom panel, the experiment is compared again to the FCHT spectrum from on-the-fly dynamics and to the Franck–Condon (FC) spectrum in Condon approximation. Note that the latter is zero because the electronic transition is symmetry forbidden. Reproduced from Aurélien Patoz, Tomislav Begušić, and Jiří Vaníček *The Journal of Physical Chemistry Letters* **9**, 2367 (2018). https://pubs.acs.org/doi/pdf/10.1021/acs.jpclett.8b00827. Requests for further reuse should be directed to the ACS.

permitted adoption of ab initio on-the-fly thawed Gaussian semiclassical dynamics with inclusion of the Herzberg–Teller approximation. The electronic excited state dynamics was performed for 2 ps with TD-DFT, B3LYP functional, and 6-31+G** basis set. DFT was employed for the optimization at the electronic ground state. The importance of a semiclassical approach able to account for the anharmonicities of the potential is pointed out in Figure 19.11, where a comparison between FCHT spectra adopting on-the-fly ab initio dynamics and the static adiabatic harmonic (AH) and vertical harmonic approximations (VH) is presented. In the AH approximation the upper electronic surface is obtained by means of a second-order expansion of the potential around the minimum, while the VH approximation is similar but based on the equilibrium configuration of the lower electronic state. The semiclassical approach outperforms the other two very clearly, with the VH approach returning very inaccurate results. Also in this application a different semiclassical approach based on a frozen Gaussian propagator and the techniques previously illustrated can be adopted.

19.11 Summary and Conclusions

In this chapter we have presented the derivation of the basic van Vleck and Heller–Herman–Kluk–Kay semiclassical propagators followed by a description of some recently developed SC techniques tailored for spectroscopy simulations. The multiple coherent states approach permits us to adopt ab initio on-the-fly molecular dynamics for semiclassical simulations with the advantage of avoiding construction of a global analytical potential energy surface. The divide-and-conquer technique allows us to investigate the quantum spectroscopic features of large molecular and supra-molecular

systems beating the so-called "curse of dimensionality". The simplified mixed semiclassical method is a promising tool that employs both frozen and thawed Gaussian semiclassical propagators to study vibrations of a molecule in a bath. Finally, some representative applications have been presented. They include power spectra of molecular and supra-molecular glycine (experimentally tagged with H_2 molecules), photoemission spectra of oligothiophenes, and the photoabsorption spectrum of benzene. In general, the described semiclassical techniques can be employed both for simulations on the electronic ground state and for calculations involving excited state dynamics.

To conclude we would like to review a few aspects of semiclassical spectroscopy that have either been recently solved or are the focus of current methodological developments. The bottleneck of semiclassical calculations lies in the determination of the Hessian matrix for the configurations visited along the trajectory, which is necessary for evolving the monodromy matrix elements and calculating the pre-exponential factor. This overhead has been alleviated by means of an interpolation scheme based on gradient estimates [64–66], and further improvements have recently led to an efficient strategy based on the dynamical construction of databases of Hessian matrices [67]. In the case of thawed Gaussian propagators, even an approximation based on a single Hessian has been recently proposed [68]. A potential issue of semiclassical simulations comes from the chaoticity of classical dynamics. Chaotic trajectories lead to a numerical loss of the unitarity of the determinant of the monodromy matrix and to unphysical values of the pre-exponential factor. This may endanger the entire calculation and often chaotic trajectories have to be discarded [20]. Some approximations to the pre-exponential factor have been proposed for overcoming this issue [69], and substantial progress on this issue has been achieved recently through development of an adiabatic switching technique for semiclassical spectroscopy [74]. As for the intensity of the calculated spectroscopic signals, apart from the possibility to simulate IR spectra starting from the dipole–dipole autocorrelation function, it is also possible to calculate them from the oscillator strengths once the wave functions are known. A procedure to determine the semiclassical wave functions expanding them on a harmonic basis set has been recently presented [70], followed by another approach capable of returning the semiclassical IR spectrum starting from power spectra even in the case of systems characterized by high densities of vibrational states [71].

Altogether we believe that semiclassical dynamics is a powerful tool for molecular spectroscopy with specific features that may make it the privileged approach for simulations of high dimensional systems. For instance, application of semiclassical spectroscopy has permitted the explaination of some features of two experiments which were left unanswered [62], while a very recent investigation focused on nucleobases [72]. Furthermore, the first calculations of vibrational semiclassical spectroscopy for molecules adsorbed on titania surfaces are now accessible [75]. We think that quantum effects should not be neglected a priori when investigating large systems spectroscopically. This is in part due to the quantum nature of spectroscopy itself and partly because of the not unusual presence of hydrogen bonds which require a quantum formalism to be described correctly. An advantage of semiclassical approaches is that they can be interfaced with ab initio molecular dynamics quite easily, since neither approximations to the potential energy nor ad hoc parameters are required. However, electronic calculations are computationally expensive and only a desirable speed up of electronic theory routines will permit employment of the highest levels of electronic theory in ab initio semiclassical simulations. Within the precision permitted by the electronic theory employed, an estimate of the accuracy of semiclassical simulations can be obtained by looking at the full width at half maximum of spectral peaks. This is generally found to be of the order of 20–25 cm^{-1} with occasional lower accuracy for particularly complex systems or spectral features, which may require further refinement. For example, a preliminary application of semiclassical spectroscopy to the Zundel cation $(H_5O_2)^+$ has demonstrated that accuracy is good even for this

Table 19.2 Principal strengths and weaknesses of semiclassical spectroscopy.

Strengths
+ Quantum effects from classical dynamics simulations.
+ Real potential energy – no approximations.
+ Interface to both analytical PESs and ab initio molecular dynamics.
+ No tunable nor ad hoc parameters.
+ Applicability to ground and excited electronic states.
+ Applicability to high dimensional systems.
Weaknesses
– Hessian calculation required.
– Classical chaotic trajectories may hamper simulations.
– Low ab initio level of electronic theory due to computational overhead.

floppy molecule [50]. A more refined and targeted study of this particular chemical species has been undertaken [76], leading to results of accuracy comparable to that of quantum calculations. A general formula to estimate the error with respect to the exact quantum mechanical result is not available, but formalisms to correct the semiclassical estimate towards the exact quantum mechanical result have been proposed by Kay and Pollak [9, 73].

Finally, we provide a brief summary of the main strengths and weaknesses of semiclassical spectroscopy, as reported in Table 19.2.

Acknowledgments

We thank past and current doctoral students and postdoctoral fellows of the Ceotto research group at Università degli Studi di Milano for their efforts and enthusiasm in developing semiclassical dynamics techniques and for revising this book chapter. In alphabetical order, they are: Dr. Chiara Aieta, Dr. Gianluca Bertaina, Dr. Max Buchholz, Dr. Marco Cazzaniga, Dr. Giovanni Di Liberto, Dr. Fabio Gabas, Dr. Huaqing Li, Dr. Ágnes Nóra Mahmoud, Dr. Marco Micciarelli, Alessandro Rognoni, and Dr. Jaime Suarez. Dr. Frank Grossmann is also warmly thanked for his careful revision. We thank Prof. Jiri Vaníček for useful discussions about the application Section. We acknowledge financial support from the European Research Council (ERC) under the European Union's Horizon 2020 research and innovation program (Grant Agreement No. [647107]– SEMICOMPLEX– ERC-2014-CoG).

Bibliography

1 Grossmann, F. (2013). *Theoretical Femtosecond Physics: Atoms and Molecules in Strong Laser Fields*. Springer.
2 Qu, C., Yu, Q., and Bowman, J.M. (2018). Permutationally invariant potential energy surfaces. *Annu. Rev. Phys. Chem.* 69 (1): 151–175.

3 Heller, E.J. (1981). The semiclassical way to molecular spectroscopy. *Acc. Chem. Res.* 14 (12): 368–375.
4 Heller, E.J. (1978). Quantum corrections to classical photodissociation models. *J. Chem. Phys.* 68 (5): 2066–2075.
5 Miller, W.H. (2005). Quantum dynamics of complex molecular systems. *Proc. Natl. Acad. Sci. U. S. A.* 102 (19): 6660–6664.
6 Miller, W.H. (2001). *J. Phys. Chem. A* 105 (13): 2942–2955.
7 Berry, M.V. and Mount, K.E. (1972). Semiclassical approximations in wave mechanics. *Rep. Prog. Phys.* 35 (1): 315.
8 Miller, W.H. (1974). Classical-limit quantum mechanics and the theory of molecular collisions. *Adv. Chem. Phys.* 25 (1): 69–177.
9 Kay, K.G. (2006). The Herman–Kluk approximation: Derivation and semiclassical corrections. *Chem. Phys.* 322 (1–2): 3–12.
10 Feynman, R.P. and Ro Hibbs, A. (1965). *Quantum Mechanics and Path Integrals*. McGraw-Hill.
11 Swenson, D. (2011). *Quantum Effects from Classical Trajectories: New Methodologies and Applications for Semiclassical Dynamics Ab initio Molecular Dynamics: Basic Theory and Advanced Methods*. Ph.D. Dissertation, University of California, Berkeley.
12 Gutzwiller, M.C. (1967). Phase-integral approximation in momentum space and the bound states of an atom. *J. Math. Phys.* 8 (10): 1979–2000.
13 John, H. and Vleck, V. (1928). The correspondence principle in the statistical interpretation of quantum mechanics. *Proc. Natl. Acad. Sci.* 14 (2): 178–188.
14 Maslov, V.P. and Fedoriuk, M.V. (1981). *Semi-Classical Approximation in Quantum Mechanics*. Boston: Reidel.
15 Miller, W.H. (1970). Classical S matrix: Numerical application to inelastic collisions. *J. Chem. Phys.* 53 (9): 3578–3587.
16 Heller, E.J. (1981). Frozen Gaussians: A very simple semiclassical approximation. *J. Chem. Phys.* 75 (6): 2923–2931.
17 Herman, M.F. and Kluk, E. (1984). A semiclasical justification for the use of non-spreading wave packets in dynamics calculations. *Chem. Phys.* 91 (1): 27–34.
18 Kay, K.G. (1994). Integral expressions for the semiclassical time-dependent propagator. *J. Chem. Phys.* 100 (6): 4377–4392.
19 Kay, K.G. (1994). Numerical study of semiclassical initial value methods for dynamics. *J. Chem. Phys.* 100 (6): 4432–4445.
20 Kay, K.G. (1994). Semiclassical propagation for multidimensional systems by an initial value method. *J. Chem. Phys.* 101 (3): 2250–2260.
21 Baranger, M., de Aguiar, M.A.M., Keck, F. et al. (2001). Semiclassical approximations in phase space with coherent states. *J. Phys. A* 34 (36): 7227.
22 Weissman, Y. (1982). Semiclassical approximation in the coherent states representation. *J. Chem. Phys.* 76 (8): 4067–4079.
23 Brewer, M.L., Hulme, J.S., and Manolopoulos, D.E. (1997). Semiclassical dynamics in up to 15 coupled vibrational degrees of freedom. *J. Chem. Phys.* 106 (12): 4832–4839.
24 Miller, W.H. (2002). An alternate derivation of the Herman Kluk (coherent state) semiclassical initial value representation of the time evolution operator. *Mol. Phys.* 100 (4): 397–400.
25 Filinov, V.S. (1986). Calculation of the Feynman integrals by means of the Monte Carlo method. *Nucl. Phys.* 271 (3): 717–725.
26 Makri, N. and Miller, W.H. (1988). Monte Carlo path integration for the real time propagator. *J. Chem. Phys.* 89 (4): 2170–2177.

27 Kluk, E., Herman, M.F., and Davis, H.L. (1986). Comparison of the propagation of semiclassical frozen Gaussian wave functions with quantum propagation for a highly excited anharmonic oscillator. *J. Chem. Phys.* 84 (1): 326–334.

28 Heller, E.J. (1981). *J. Chem. Phys.* 94 (4): 2723–2729.

29 Zambrano, E., uc, M., and Vaníček, J. (2013). Improving the accuracy and efficiency of time-resolved electronic spectra calculations: Cellular dephasing representation with a prefactor. *J. Chem. Phys.* 139 (5): 054109.

30 uc, M. and Vaníček, J. (2012). Accelerating the calculation of time-resolved electronic spectra with the cellular dephasing representation. *Mol. Phys.* 110 (9-10): 945–955.

31 Wang, H., Manolopoulos, D.E., and Miller, W.H. (2001). Generalized Filinov transformation of the semiclassical initial value representation. *J. Chem. Phys.* 115 (14): 6317–6326.

32 urch, M.S., Antipov, S.V., and Ananth, N. (2017). Validating and implementing modified Filinov phase filtration in semiclassical dynamics. *J. Chem. Phys.* 146 (23): 234104.

33 Elran, Y. and Kay, K.G. (1999). Improving the efficiency of the Herman–Kluk propagator by time integration. *J. Chem. Phys.* 110 (8): 3653–3659.

34 Elran, Y. and Kay, K.G. (1999). Time-integrated form of the semiclassical initial value method. *J. Chem. Phys.* 110 (18): 8912–8918.

35 Kaledin, A.L. and Miller, W.H. (2003). Time averaging the semiclassical initial value representation for the calculation of vibrational energy levels. *J. Chem. Phys.* 118 (16): 7174–7182.

36 Kaledin, A.L. and Miller, W.H. (2003). *J. Chem. Phys.* 119 (6): 3078–3084.

37 Tamascelli, D., Dambrosio, F.S., Conte, R., and Ceotto, M. (2014). Graphics processing units accelerated semiclassical initial value representation molecular dynamics. *J. Chem. Phys.* 140 (17): 174109.

38 Pratihar, S., Ma, X., Homayoon, Z. et al. (2017). Direct chemical dynamics simulations. *J. Am. Chem. Soc.* 139 (10): 3570–3590.

39 Ceotto, M., Atahan, S., Tantardini, G.F., and Aspuru-Guzik, A. (2009). Multiple coherent states for first-principles semiclassical initial value representation molecular dynamics. *J. Chem. Phys.* 130 (23): 234113.

40 De Leon, N. and Heller, E.J. (1983). Semiclassical quantization and extraction of eigenfunctions using arbitrary trajectories. *J. Chem. Phys.* 78: 4005–4017.

41 Ceotto, M., Tantardini, G.F., and Aspuru-Guzik, A. (2011). Fighting the curse of dimensionality in first-principles semiclassical calculations: Non-local reference states for large number of dimensions. *J. Chem. Phys.* 135 (21): 214108.

42 Ceotto, M., Dell' Angelo, D., and Tantardini, G.F. (2010). Multiple coherent states semiclassical initial value representation spectra calculations of lateral interactions for CO on Cu (100). *J. Chem. Phys.* 133 (5): 054701.

43 Ceotto, M., Valleau, S., Tantardini, G.F., and Aspuru-Guzik, A. (2011). First principles semiclassical calculations of vibrational eigenfunctions. *J. Chem. Phys.* 134 (23): 234103.

44 Ceotto, M., Atahan, S., Shim, S. et al. (2009). First-principles semiclassical initial value representation molecular dynamics. *Phys. Chem. Chem. Phys.* 11: 3861–3867.

45 Dressler, S. and Thiel, W. (1997). Anharmonic force fields from density functional theory. *Chem. Phys. Lett.* 273 (1): 71–78.

46 Conte, R., Aspuru-Guzik, A., and Ceotto, M. (2013). Reproducing deep tunneling splittings, resonances, and quantum frequencies in vibrational spectra from a handful of direct ab initio semiclassical trajectories. *J. Phys. Chem. Lett.* 4 (20): 3407–3412.

47 Gabas, F., Conte, R., and Ceotto, M. (2017). On-the-fly ab initio semiclassical calculation of glycine vibrational spectrum. *J. Chem. Theory Comput.* 13: 2378.

48 Wehrle, M., Sulc, M., and Vanicek, J. (2014). On-the-fly ab initio semiclassical dynamics: Identifying degrees of freedom essential for emission spectra of oligothiophenes. *J. Chem. Phys.* 140 (24): 244114.

49 Ceotto, M., Di Liberto, G., and Conte, R. (2017). Semiclassical "Divide-and-Conquer" method for spectroscopic calculations of high dimensional molecular systems. *Phys. Rev. Lett.* 119 (1): 010401.

50 Di Liberto, G., Conte, R., and Ceotto, M. (2018). "divide and conquer" semiclassical molecular dynamics: A practical method for spectroscopic calculations of high dimensional molecular systems. *J. Chem. Phys.* 148 (1): 014307.

51 Di Liberto, G., Conte, R., and Ceotto, M. (2018). "divide-and-conquer" semiclassical molecular dynamics: An application to water clusters. *J. Chem. Phys.* 148 (10): 104302.

52 Heller, E.J. (1975). Time dependent approach to semiclassical dynamics. *J. Chem. Phys.* 62 (4): 1544–1555.

53 Buchholz, M., Grossmann, F., and Ceotto, M. (2016). Mixed semiclassical initial value representation time-averaging propagator for spectroscopic calculations. *J. Chem. Phys.* 144: 094102.

54 Grossmann, F. (2006). A semiclassical hybrid approach to many particle quantum dynamics. *J. Chem. Phys.* 125 (1).

55 Buchholz, M., Grossmann, F., and Ceotto, M. (2017). Application of the mixed time-averaging semiclassical initial value representation method to complex molecular spectra. *J. Chem. Phys.* 147 (16): 164110.

56 Buchholz, M., Grossmann, F., and Ceotto, M. (2018). Simplified approach to the mixed time-averaging semiclassical initial value representation for the calculation of dense vibrational spectra. *J. Chem. Phys.* 148 (11): 114107.

57 Valiev, M., Bylaska, E.J., Govind, N. et al. (2010). NWChem: A comprehensive and scalable open-source solution for large scale molecular simulations. *Comput. Phys. Commun.* 181 (9): 1477–1489.

58 Lourderaj, U., Sun, R., Kohale, S.C. et al. (2014). The venus/nwchem software package. tight coupling between chemical dynamics simulations and electronic structure theory. *Comput. Phys. Commun.* 185 (3): 1074–1080.

59 Ma, X., Di Liberto, G., Conte, R. et al. (2018). A quantum mechanical insight into [illegible] reactions: Semiclassical initial value representation calculations of vibrational features of the cl-ch3cl pre-reaction complex with the venus suite of codes. *J. Chem. Phys.* 149 (16): 164113.

60 Stepanian, S.G., Reva, I.D., Radchenko, E.D. et al. (1998). Matrix-isolation infrared and theoretical studies of the glycine conformers. *J. Phys. Chem. A* 102 (6): 1041–1054.

61 Masson, A., Williams, E.R., and Rizzo, T.R. (2015). Molecular hydrogen messengers can lead to structural infidelity: A cautionary tale of protonated glycine. *J. Chem. Phys.* 143 (10): 104313.

62 Gabas, F., Di Liberto, G., Conte, R., and Ceotto, M. (2018). Protonated glycine supramolecular systems: the need for quantum dynamics. *Chem. Sci.* 9: 7894–7901.

63 Patoz, A., Begusic, T., and Vanicek, J. (2018). On-the-fly ab initio semiclassical evaluation of absorption spectra of polyatomic molecules beyond the condon approximation. *J. Phys. Chem. Lett.* 9 (9): 2367–2372.

64 Wu, H., Rahman, M., Wang, J. et al. (2010). Higher-accuracy schemes for approximating the hessian from electronic structure calculations in chemical dynamics simulations. *J. Chem. Phys.* 133 (7): 074101.

65 Zhuang, Y., Siebert, M.R., Hase, W.L. et al. (2012). Evaluating the Accuracy of Hessian Approximations for Direct Dynamics Simulations. *J. Chem. Theory Comput.* 9 (1): 54–64.

66 Ceotto, M., Zhuang, Y., and Hase, W.L. (2013). Accelerated direct semiclassical molecular dynamics using a compact finite difference Hessian scheme. *J. Chem. Phys.* 138 (5): 054116.

67 Conte, R., Gabas, F., Botti, G. et al. (2019). Semiclassical vibrational spectroscopy with hessian databases. *J. Chem. Phys.* 150: 244118.

68 Begusic, T., Cordova, M., and Vanicek, J. (2019). Single-hessian thawed gaussian approximation. *J. Chem. Phys.* 150 (15): 154117.

69 Di Liberto, G. and Ceotto, M. (2016). The importance of the pre-exponential factor in semiclassical molecular dynamics. *J. Chem. Phys.* 145: 144107.

70 Micciarelli, M., Conte, R., Suarez, J., and Ceotto, M. (2018). Anharmonic vibrational eigenfunctions and infrared spectra from semiclassical molecular dynamics. *J. Chem. Phys.* 149: 064115.

71 Micciarelli, M., Gabas, F., Conte, R., and Ceotto, M. (2019). An effective semiclassical approach to ir spectroscopy. *J. Chem. Phys.* 150 (18): 184113.

72 Gabas, F., Di Liberto, G., and Ceotto, M. (2019). Vibrational investigation of nucleobases by means of divide-and-conquer semiclassical dynamics. *J. Chem. Phys.* 150: 224107.

73 Pollak, E. (2007). *The Semiclassical Initial Value Series Representation of the Quantum Propagator*, 259–271. Berlin, Heidelberg: Springer Berlin Heidelberg.

74 Conte, R., Parma, L., Aieta, C. et al. (2019). Improved semiclassical dynamics through adiabatic switching trajectory sampling. *J. Chem. Phys.* 151: 214107.

75 Cazzaniga, M., Micciarelli, M., Moriggi, F. et al. (2020). Anharmonic calculations of vibrational spectra for molecular adsorbates: A divide-and-conquer semiclassical molecular dynamics approach. *J. Chem. Phys.* 152: 104104.

76 Bertaina, G., Di Liberto, G., and Ceotto, M. (2019). Reduced rovibrational coupling aCrtesian dynamics for semiclassical calculations: Application to the spectrum of the Zundel cation. *J. Chem. Phys.* 151: 114307.